Article

Cell

Differences in Tumor Microenvironment Dictate T Helper Lineage Polarization and Response to Immune Checkpoint Therapy

Graphical Abstract

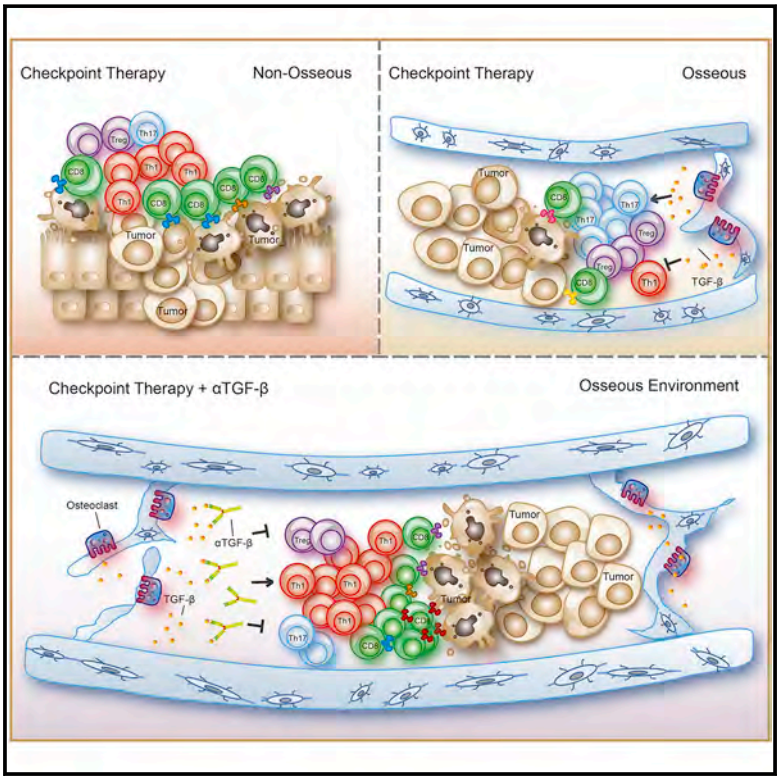

Highlights

- Lack of T_h1 cells in the tumor confers resistance to immune checkpoint therapy
- High TGF-β amounts in prostate cancer bone metastases restrains the T_h1 lineage and hinders ICT
- Tumors in the bone promote osteoclast-mediated bone resorption that releases TGF-β
- TGF-β inhibition allows T_h1 development and augments ICT in bone prostate cancer

Authors

Shiping Jiao, Sumit K. Subudhi, Ana Aparicio, Zhongqi Ge, Baoxiang Guan, Yuji Miura, Padmanee Sharma

Correspondence

padsharma@mdanderson.org

In Brief

The response to immune checkpoint therapy in a subset of patients with castration-resistant prostate cancer who develop bone metastases can be improved by promoting CD4 T_h1 effector T cell responses and clonal expansion of CD8 T cells through TGF-β blockade

Jiao et al., 2019, Cell *179*, 1177–1190
November 14, 2019
https://doi.org/10.1016/j.cell.2019.10.029

CellPress

Cell

Differences in Tumor Microenvironment Dictate T Helper Lineage Polarization and Response to Immune Checkpoint Therapy

Shiping Jiao,[1,3] Sumit K. Subudhi,[1] Ana Aparicio,[1] Zhongqi Ge,[2] Baoxiang Guan,[1] Yuji Miura,[1] and Padmanee Sharma[1,2,3,4,*]

[1]Department of Genitourinary Medical Oncology, The University of Texas MD Anderson Cancer Center, Houston, TX 77030, USA
[2]Department of Immunology, The University of Texas MD Anderson Cancer Center, Houston, TX 77030, USA
[3]Graduate School of Biomedical Sciences, The University of Texas MD Anderson Cancer Center UTHealth, Houston, TX 77030, USA
[4]Lead Contact
*Correspondence: padsharma@mdanderson.org
https://doi.org/10.1016/j.cell.2019.10.029

SUMMARY

Immune checkpoint therapy (ICT) shows encouraging results in a subset of patients with metastatic castration-resistant prostate cancer (mCRPC) but still elicits a sub-optimal response among those with bone metastases. Analysis of patients' bone marrow samples revealed increased T_h17 instead of T_h1 subsets after ICT. To further evaluate the different tumor microenvironments, we injected mice with prostate tumor cells either subcutaneously or intraosseously. ICT in the subcutaneous CRPC model significantly increases intra-tumoral T_h1 subsets and improves survival. However, ICT fails to elicit an anti-tumor response in the bone CRPC model despite an increase in the intra-tumoral CD4 T cells, which are polarized to T_h17 rather than T_h1 lineage. Mechanistically, tumors in the bone promote osteoclast-mediated bone resorption that releases TGF-β, which restrains T_h1 lineage development. Blocking TGF-β along with ICT increases T_h1 subsets and promotes clonal expansion of CD8 T cells and subsequent regression of bone CRPC and improves survival.

INTRODUCTION

Immune checkpoint therapy (ICT) is an immunotherapeutic modality that targets cytotoxic lymphocyte antigen-4 (CTLA-4), programmed cell death protein 1 (PD-1), or programmed death ligand 1 (PD-L1) and reverses the immunosuppressive state by reactivating anti-tumor T cells, including CD4 T_h1 effector T cells and CD8 cytotoxic T lymphocytes (CTLs) (Dong et al., 2002; Leach et al., 1996). Monoclonal antibodies against these immune checkpoint targets have shown encouraging results across a spectrum of tumors. For example, blocking either CTLA-4 or PD-1 in patients with metastatic melanoma resulted in object response rates ranging from 20% to 45% (Hodi et al., 2010), whereas up to 60% response rate was observed upon dual checkpoint blockade with anti-CTLA-4 plus anti-PD-1 (Larkin et al., 2015; Wolchok et al., 2017). The therapeutic efficacy of ICT depends on the expansion of intra-tumoral CD4 T_h1 lineage cells, the activation of cytotoxic CD8 T cells, and the generation of long-term memory T cells (Chen et al., 2009; Liakou et al., 2008; Wei et al., 2017). On the basis of the concept of targeting T cells, as opposed to tumor cells, ICT has been FDA-approved or is being developed as treatment for multiple tumor types such as lung, bladder, gastric, kidney, and many other cancers (Fuchs et al., 2018; Hellmann et al., 2017; Patel et al., 2018).

Prostate cancer is the most common malignancy diagnosed in men (Siegel et al., 2012). Despite a rapid initial response to androgen deprivation therapy, the majority of prostate cancer patients eventually progress to lethal metastatic castration-resistant prostate cancer (mCRPC), and bone is the most common site of metastases (70%–80%) (Halabi et al., 2016). In a previous phase III trial of ipilimumab versus placebo in patients with mCRPC, those with bone metastases responded poorly compared with those without bone metastases (Beer et al., 2017). More recently, in a phase II trial (NCT02985957) conducted on patients with mCRPC, ICT elicited prostate-specific antigen (PSA) responses in only 1 of 24 (4%) patients with bone metastases as compared with PSA responses in 9 of 50 (18%) patients without bone metastases (Sharma et al., 2019).

The sub-optimal response of CRPC bone metastases to ICT suggests a distinct immunological niche in the bone microenvironment compared with that of soft tissue metastases. To test this hypothesis and identify underlying mechanisms, we compared pre- and post-treatment bone marrow tissues from patients with mCRPC to the bone from patients who were treated with ipilimumab in two clinical trials (NCT02985957 and NCT02703623). In addition, we established murine osseous and non-osseous (subcutaneous) CRPC models and performed high-dimensional single-cell analysis with mass cytometry (CyTOF), single-cell RNA sequencing (scRNA-seq), single-cell T cell receptor sequencing (TCR-seq), and multiplex cytokine profiling to identify the distinct immune cell subsets and cytokine environment in the tumor lesions. On the basis of our findings, we devised and evaluated an organ-specific strategy of targeting the microenvironment associated with bone metastases to improve anti-tumor responses with ICT.

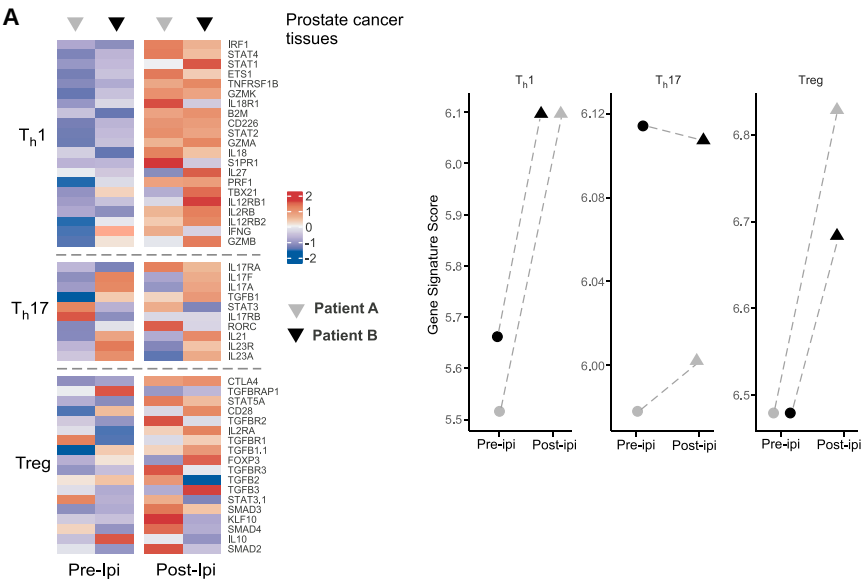

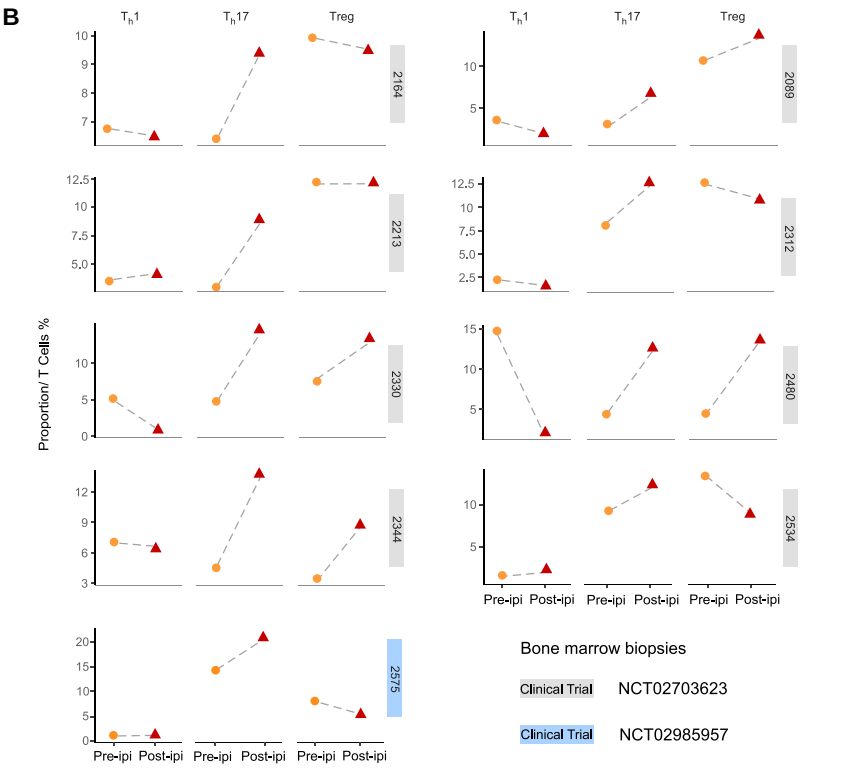

Figure 1. Ipilimumab Induces T_h17 as Opposed to T_h1 Lineage Expansion in Bone Metastases from Patients with Prostate Cancer

(A) Comparison of the CD4 T cell lineage gene signatures of paired pre- and post-ipilimumab prostate cancer tissues. Gene signature scores in the right image were calculated using the mean expression of the marker genes in each category (T_h1, T_h17, and Treg) for each sample.

(B) Immune cell subsets of paired pre- and post-ipilimumab bone marrow tissues of nine patients with clinically confirmed bone metastases from two clinical trials (NCT02703623 and NCT02985957). See also Table S1. CD4 lineages were defined as follows: T_h1, $CD3^+CD4^+TBX21^+$; T_h17, $CD3^+CD4^+ROR\gamma t^+$; Treg, $CD3^+CD4^+Foxp3^+$. The phenotypic markers and percentage of each cell subset in each sample are shown in Figure S1.

RESULTS

Ipilimumab Induced T_h17 as Opposed to T_h1 Lineage Expansion in Bone Metastases from Patients with Prostate Cancer

ICT is known to expand intra-tumoral CD4 T_h1 effector cells in multiple tumor types involving soft tissues, as published for both animal models and patient samples (Chen et al., 2009; Liakou et al., 2008; Wei et al., 2017). Consistent with these data, we observed an enhanced T_h1 subset signature in paired pre- and post-treatment primary soft-tissue prostate tumors of patients treated with ipilimumab (NCT01194271) (Figure 1A). In contrast, when we compared nine paired pre- and post-treatment bone marrow samples from ipilimumab-treated patients with bone mCRPC (NCT02703623 and NCT02985957) (Table S1), we observed a significant increase in T_h17 cells but not in T_h1 effector cells (Figures 1B and S1). The absence of an increase in T_h1 lineage in bone metastatic sites after ICT suggests a distinct tumor microenvironment in the bone as compared to soft tissue, which we surmised was a mechanistic basis for the resistance to ICT.

Immune Checkpoint Therapy Shows Minimal Therapeutic Effects in Murine Bone CRPC Model Despite an Increase in Intra-tumoral T Cells

We established a mouse model of bone CRPC by intraosseous injection of syngeneic Myc-CaP prostate cancer cells (Figure 2A), followed by degarelix administration, a gonadotropin-releasing hormone (GnRH) antagonist that induces castrate levels of serum testosterone within 3 days (Figure S2A). The castration state lasted for 28 days, during which the tumor lesions continued to grow (Figures S2B and S2C), indicating successful induction of a model for CRPC. This murine model of prostate cancer was used to represent mCRPC to the bones.

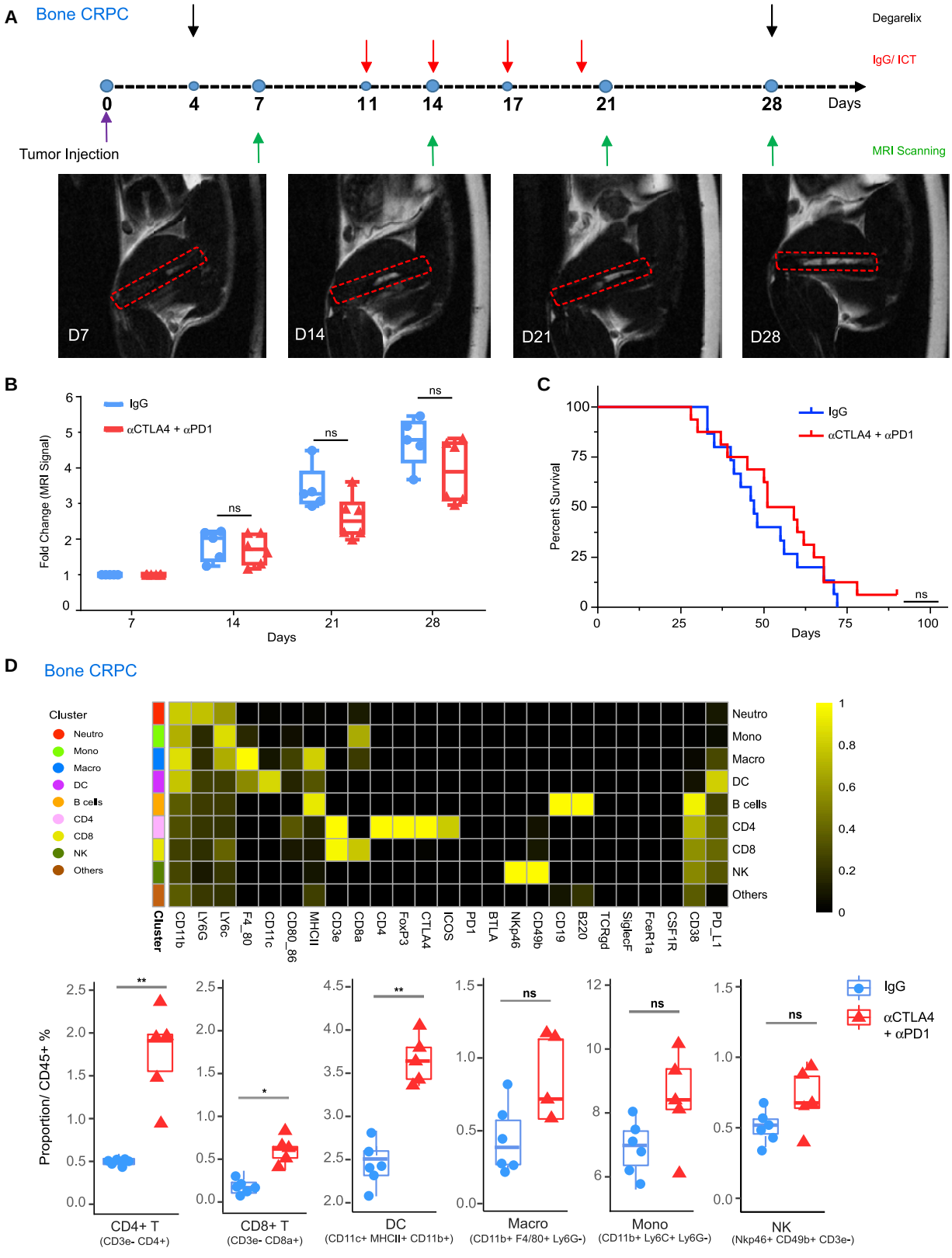

(legend on next page)

In addition, we established a subcutaneous CRPC murine model to mimic human CRPC in the primary prostate or metastases to a soft tissue (Figure S3A). The combination of anti-CTLA-4 plus anti-PD-1 antibodies had minimal effects on the tumor volume and overall survival of mice bearing the bone CRPC lesions (Figures 2B and 2C). In contrast, the combination induced significant regression of the subcutaneous CRPC and improved overall survival (Figure S3A and S3B). This is consistent with the clinical observation that ICT elicits a sub-optimal response in bone mCRPC as compared to soft-tissue mCRPC.

We next profiled and compared the pre- and post-treatment tumor infiltrating $CD45^+$ immune cell subsets in both the bone and subcutaneous CRPC models. ICT resulted in a significant increase in the proportion of CD4 T cells, CD8 T cells, and dendritic cells (DCs) in bone as well as subcutaneous CRPC (Figures 2D and S3C), which is consistent with previous findings of ICT-induced expansion of tumor-infiltrating T cells. Altogether, although ICT successfully expanded tumor-infiltrating T cells in both bone and subcutaneous CRPC, it failed to significantly inhibit growth of bone tumors.

Lack of T_h1 Polarization in Murine Bone CRPC

Next, we profiled $CD3\varepsilon^+CD11b^-$ cells in bone CRPC by CyTOF, focusing on T cell subsets. The tumor-infiltrating T cells were divided into 15 clusters (Figure S4A), which were functionally annotated to 5 subsets: T_h17 ($CD4^+IL17A^+Foxp3^-IFN\gamma^-$), Treg cells ($CD4^+Foxp3^+$), CD8 T cells ($CD3\varepsilon^+CD8a^+$), $TCR\gamma\delta$ cells ($CD3\varepsilon^+TCR\gamma\delta^+$), and natural killer (NK) T cells ($CD3\varepsilon^+CD49b^+NKp46^-$) (Figure 3A). The CD4 T cells in the bone CRPC model consisted of only T_h17 and Treg lineages, and there was an absence of T_h1 effector cells ($CD4^+IFN\gamma^+Foxp3^-$) despite treatment with ICT (Figures 3A and 3B). Moreover, in the bone CRPC model, we found that T_h17 cells increased significantly after ICT (Figures 3B and 3E). In contrast, in the subcutaneous CRPC model, T_h1 cells were detected prior to the treatment (Figure 3C) and increased significantly after ICT, along with a decrease in T_h17 and Treg cells (Figures 3D and 3E). Altogether, lack of T_h1 effector lineage in the tumor microenvironment is a distinctive feature of bone CRPC and is possibly responsible for the poor response to ICT.

Aberrantly High TGF-β1 as a Distinct Cytokine Signature in Bone CRPC

The lack of T_h1 lineage in the bone CRPC suggests a distinct cytokine profile within the tumor-bearing bone microenvironment. Therefore, using bone marrow samples from tumor-bearing femurs and contralateral tumor-free femurs, we analyzed the levels of 13 cytokines associated with T cell lineage development: interleukin-2 (IL-2), IL-4, IL-5, IL-6, IL-9, IL-10, IL-12/p70, IL-17A, IL-21, IL-23, interferon-γ (IFN-γ), tumor necrosis factor-α (TNF-α), and free active transforming growth factor-β1 (TGF-β1) (Figure 4A). TGF-β1 levels were significantly elevated in tumor-bearing bone marrow supernatants as compared with contralateral non-tumor-bearing samples regardless of whether the mice received ICT or immunoglobulin G (IgG) control (Figures 4A and S5A). Given that TGF-β1 restrains T_h1 lineage development (Lin et al., 2005; Park et al., 2005) but drives both T_h17 and Treg polarization (Fu et al., 2004; Mangan et al., 2006), its high amounts in the bone tumor microenvironment can explain, at least partly, the high proportion of T_h17 and Treg subsets in the bone CRPC model. T_h17 polarization also requires the presence of IL-6 (Mangan et al., 2006; Veldhoen et al., 2006), which was detected in both tumor-bearing and tumor-free supernatants. However, IL-6 amounts in the bone marrow supernatant were significantly higher than that in the serum, regardless of tumor-bearing status (Figure S5B), which provides a possible explanation for the T_h17 lineage polarization observed in the bone tumor microenvironment. Given that IL-6 is an osteogenic cytokine secreted by a variety of cells in the bone marrow, such as stromal cells and osteoblasts (Chiu et al., 1988; Ishimi et al., 1990), its higher endogenous levels in the bone marrow is expected. In contrast, the TGF-β amounts were increased significantly in the tumor-bearing supernatants but were only slightly higher in the tumor-free supernatants than in the sera (Figure S5C).

To further evaluate the distinct cytokine environment in the bone tumors, we established a dual subcutaneous and intraosseous prostate tumor model and profiled 13 cytokines in the sera and supernatants from soft-tissue and bone tumors (Figures 4B and S5D). TGF-β1 and IL-6 amounts in the osseous environment were significantly higher than in the non-osseous environment (Figure 4B). These findings indicate that high TGF-β1 amounts is a distinct cytokine in bone CRPC that might act to restrain T_h1 polarization. The presence of TGF-β1 and IL-6 might expand CD4 T cells toward a T_h17 lineage as opposed to a T_h1 lineage in the osseous tumor microenvironment.

Enhanced Osteoclastic Activity in Bone CRPC Increases TGF-β1

Although previous studies have reported that prostate tumors can secrete TGF-β1, the significant increase observed in the tumor microenvironment (Figure 4A) indicates an additional source in bone CRPC. Given that tumor metastases to the bone is often accompanied by abnormal bone remodeling (Figure S6A) and the bone matrix is a major reservoir of TGF-β1, we hypothesized that remodeling of the bone matrix is responsible for the aberrantly high TGF-β1 amounts in bone CRPC. To test this hypothesis, we compared the extent of mineralization and the osteoblastic and osteoclastic activities in the tumor-bearing and

Figure 2. Murine Bone CRPC Tumors Have Minimal Response after Blockade of CTLA-4 and PD-1

(A) Schematic diagram showing the treatment regimen, schedule, and the representative MRI scans of tumor-bearing bones in the bone CRPC model.

(B and C) Comparison of tumor volume (B) and overall survival (C) of the treated and untreated mice with bone CRPC. Tumor in the bone were visualized using MRI and the tumor volume was evaluated using the ImageJ program. In (B), $^*p < 0.05$, $^{**}p < 0.01$, $^{***}p < 0.001$; ns, not significant.

(D) CyTOF mapping of $CD45^+$ tumor-infiltrating lymphocyte subsets in bone CRPC. At the top is a heatmap showing the immuno-phenotype of each annotated subset. On the bottom is the frequency of each annotated subset in individual IgG- and ICT-treated mice. Data are represented as median ± interquartile range. The tumor tissues for CyTOF analysis were obtained from the mice 3 days after the last dose of a 3-dose IgG or ICT regimen. $^*p < 0.05$, $^{**}p < 0.01$, $^{***}p < 0.001$; ns, not significant. See also Figures S2 and S3.

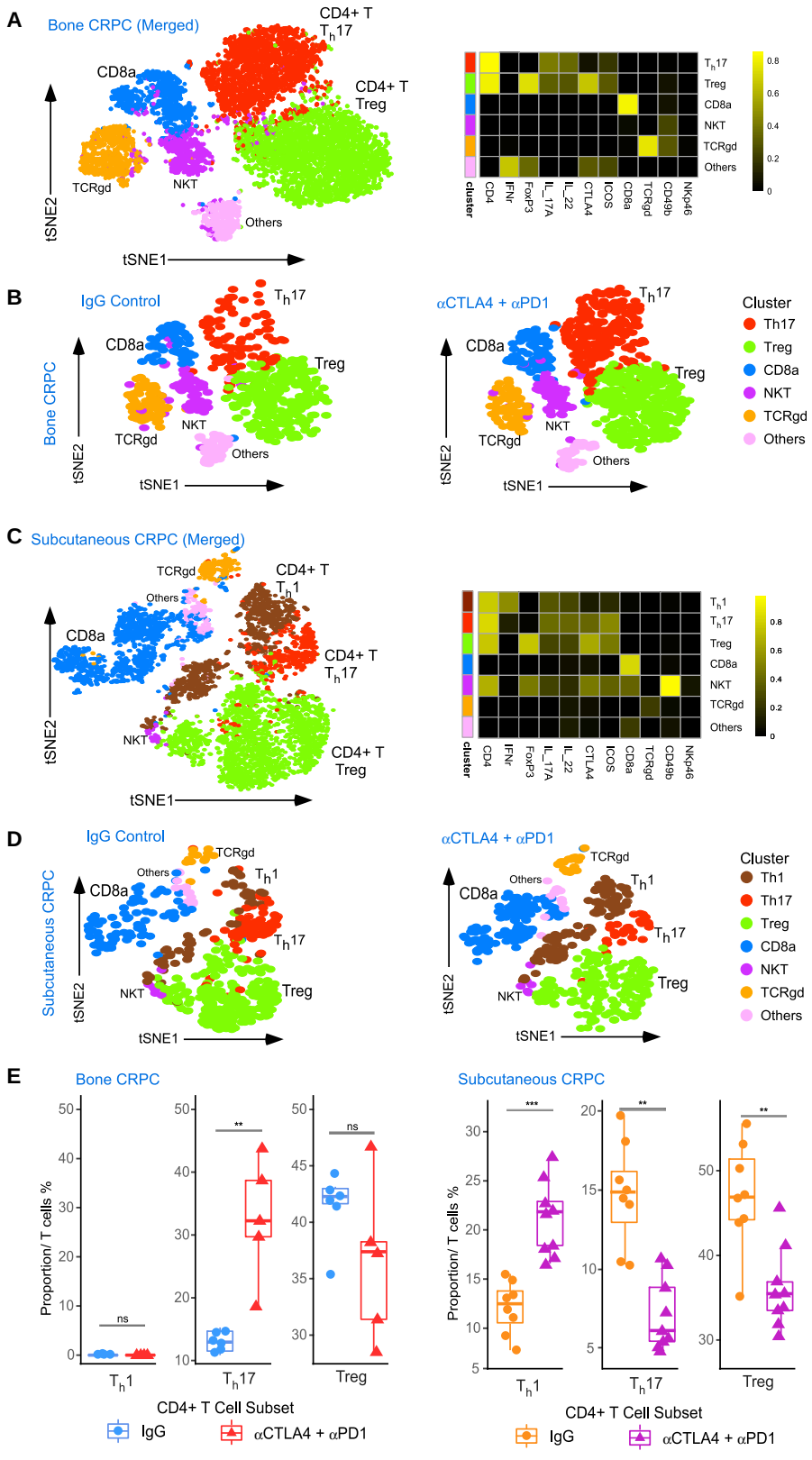

(legend on next page)

contralateral tumor-free femur sections by using Von Kossa, toluidine blue, and tartrate-resistant acid phosphatase (TRAP) staining. The tumor-free femur consisted of well-organized cancellous and cortical bone tissues with clear lamellar structure, indicating a functional balance between the osteoblasts and osteoclasts. In contrast, this balance was disrupted in tumor-bearing bones, which showed atrophy of the distal epiphysis and growth plate, as well as areas of unorganized woven matrix. The tumor-bearing bones consisted of highly proliferative $TRAP^+$ multinucleated osteoclasts and metastasized tumor cells (Figure S6B). Therefore, tumors in the bone triggers osteoclast activation, which significantly erodes the residual bone surface, resulting in extensive bone resorption. To substantiate that osteoclast-induced bone resorption releases excessive amounts of TGF-β1 into the tumor microenvironment, we inhibited the osteoclasts in the tumor-bearing bone by blocking receptor activator of nuclear factor κ-B ligand (RANKL), a key factor regulating osteoclast differentiation and activation (Boyce and Xing, 2008). Anti-RANKL therapy successfully reduced osteoclastic activities and likely skewed bone remodeling toward the osteoblastic activities (Figure 4C). In addition, blocking RANKL also significantly diminished TGF-β1 amounts in the tumor-bearing femur without affecting the other cytokines (Figures 4D and S6C). Altogether, osteoclast-mediated bone resorption appears to be the primary source of TGF-β1 in the bone CRPC microenvironment.

To test our hypothesis in human subjects, we compared TGF-β1 amounts in the bone marrow supernatants of healthy donors and prostate cancer patients with and without bone metastases (clinical trial NCT02703623). No significant difference was observed between the patients without bone metastases and the healthy donors, whereas patients with bone metastases showed aberrantly high TGF-β1 amounts in the osseous environment (Figure S6D).

TGF-β Blockade Potentiates Immune Checkpoint Therapy by Restoring T_h1 Lineage Polarization

The distinct cytokine profile of the bone CRPC microenvironment is a combination of a significant elevation in TGF-β amounts after metastasis and the physiologically high amounts of IL-6 in the bone marrow. ICT expands the tumor-infiltrating CD4 T cells and DCs, which are essential for T cell priming. However, high TGF-β and IL-6 amounts appear to skew the newly primed CD4 T cells toward a T_h17 lineage instead of T_h1 lineage, thereby restricting development of T_h1 effector cells, which are critical for ICT-induced anti-cancer immunity. On the basis of these data, we tested the efficacy of combining ICT with anti-TGF-β, anti-RANKL, or anti-IL-6 antibodies in the bone CRPC model. Inclusion of anti-TGF-β significantly contributed to ICT-mediated tumor growth suppression and overall survival; however, blocking RANKL or IL-6 had less pronounced benefits (Figures 5A, 5B, and S6E). Dual targeting CTLA-4 and PD-1 is associated with higher frequency of toxicities in patients than in mice (Larkin et al., 2015; Sharma et al., 2019), and the additional blockade of TGF-β, whose pivotal role is to maintain immune tolerance, can amplify the toxicity (Shull et al., 1992). To propose a potential combination strategy with a manageable toxicity profile in the clinic, we tested the efficacy of simultaneously blocking CTLA-4 and TGF-β. This novel combination significantly suppressed bone CRPC progression and improved overall survival as compared with monotherapies (Figures 5C, 5D, and S6F).

To demonstrate the effects of TGF-β blockade on the reshaping of T cell lineages, we profiled the tumor infiltrating T cells from bone CRPC after mono- or combination therapy via CyTOF analysis. Consistent with our previous results, T_h1 cells were rare in bone CRPC samples despite CTLA-4 blockade (Figures 5E and 5F); however, combination therapy with anti-CTLA-4 plus anti-TGF-β significantly increased the frequency of T_h1 cells while concomitantly decreasing the frequency of Tregs (Figure 5F).

TGF-β Blockade Augments Antigen-Specific Effector-Memory CD8 T Cell Clonal Expansion in Bone CRPC

Cytotoxic CD8 T cells play a direct role in tumor cell killing, and their activation is dependent on the CD4 T_h1 lineage (Janssen et al., 2003). We found that the addition of TGF-β blockade to ICT induces T_h1 lineage in bone CRPC, which creates a conducive environment for CD8 T cell activation. Although an increase in the intra-tumoral CD8 T cell population is usually a sign of immune recognition and activation, recent studies have shown that the majority of tumor-infiltrating CD8 T cells is comprised of unique TCR clones and non-tumor reactive bystanders (Scheper et al., 2019; Simoni et al., 2018). Therefore, clonal expansion of intra-tumoral CD8 T cells is a more accurate marker for tumor recognition and anti-tumor immune activation. We performed single-cell RNA and T cell receptor (TCR) sequencing to obtain the complete transcriptome data along with paired TCR information of each CD8 T cell, which allowed us to gain insights into the functional states of and clonal relationship among the intra-

Figure 3. Lack of T_h1 Lineage in Bone CRPC Tumors

(A) CyTOF mapping of tumor-infiltrating $CD3\varepsilon^+CD11b^-$ T cells in bone and subcutaneous CRPC. On the left is a tSNE visualization of the annotated T cell lineages. On the right is a heatmap showing immuno-phenotype of each annotated lineage. See also Figure S4 for the heatmaps and tNE of the 15 unannotated clusters generated by FlowSOM.

(B) Representative tSNE of tumor-infiltrating T cell lineages in IgG- or ICT-treated bone CRPC. Samples for CyTOF analysis were obtained from the mice 3 days after the last dose of a total of 3 doses of IgG or ICT regimen. The tumor tissues for CyTOF analysis were obtained from the mice 3 days after the last dose of a 3-dose IgG or ICT regimen.

(C) CyTOF mapping of tumor-infiltrating $CD3\varepsilon^+$ $CD11b^-$ T cells in subcutaneous CRPC. On the left is a tSNE visualization of the annotated T cell lineages. On the right is a heat map showing immuno-phenotype of each annotated lineage. See also Figure S4 for the heat maps and TSNE of the 15 unannotated clusters generated by FlowSOM.

(D) Representative tSNE of tumor-infiltrating T cell lineages in IgG- or ICT-treated subcutaneous CRPC. Samples for CyTOF analysis were obtained from the mice 3 days after the last dose of a total of 3 doses of IgG or ICT regimen.

(E) Proportion of annotated CD4 T_h lineages in individual IgG- and ICT-treated bone and subcutaneous CRPC. Data are represented as median ± interquartile range in the boxplots. *$p < 0.05$, **$p < 0.01$, ***$p < 0.001$; ns, not significant.

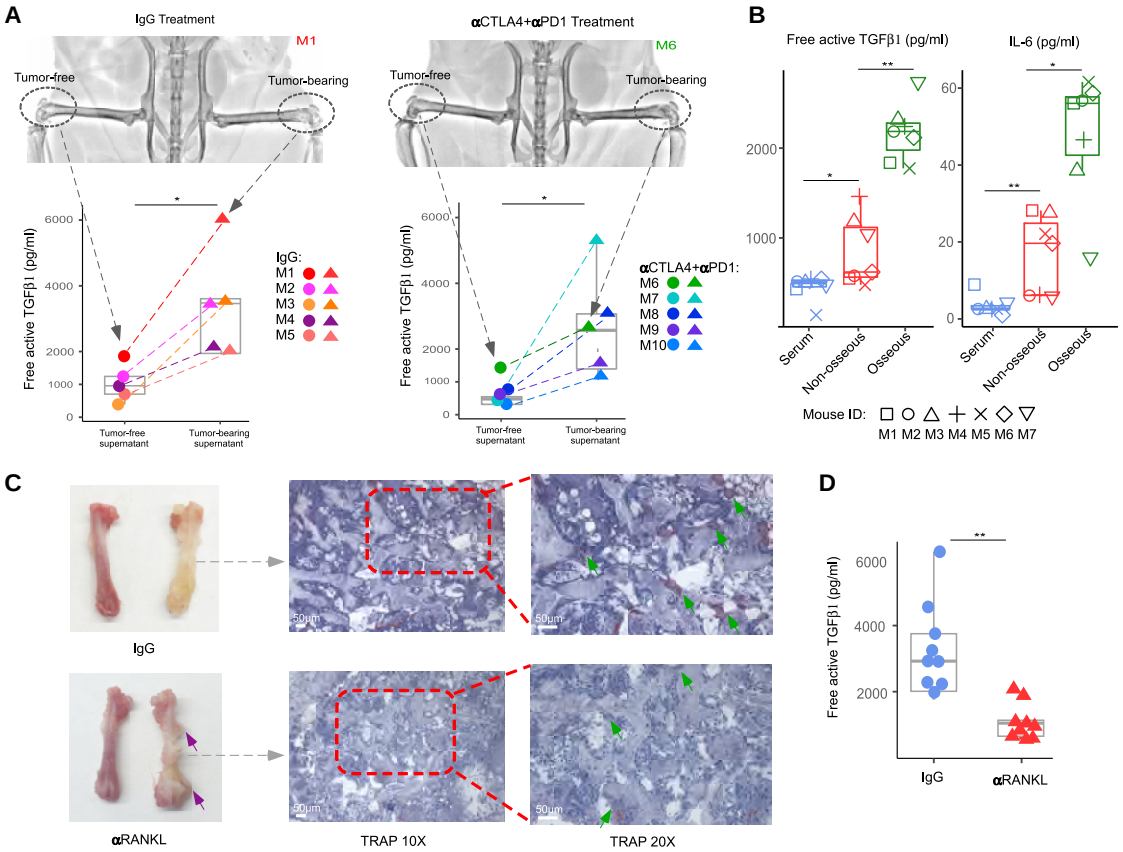

Figure 4. Increased Osteoclastic Activity Elevates TGF-β1 in the Microenvironment of Bone CRPC Tumors

(A) At the top are femur radiographs displaying the anatomical location of tumor-bearing and contralateral tumor-free femurs of IgG- or ICT-treated mice. Shown on the bottom are TGF-β1 amounts in the supernatants of tumor-bearing and contralateral tumor-free bone marrow of individual IgG- and ICT-treated mice. Data of the remaining cytokines are shown in Figure S5A. *p < 0.05, **p < 0.01, ***p < 0.001; ns, not significant.

(B) TGF-β1 and IL-6 amounts in the supernatants of tumor-bearing bone marrow and subcutaneous prostate tumors, and the serum of the same mouse (n = 7). Non-osseous: the supernatants of subcutaneous prostate tumors. Osseous: the supernatants of bone tumors. Data of the remaining cytokines are shown in Figure S5D. *p < 0.05, **p < 0.01, ***p < 0.001; ns, not significant.

(C) On the left are macroscopic images of tumor-bearing and contralateral tumor-free femurs of the IgG- and anti-RANKL-treated mice. The purple arrows indicate the accumulation of newly formed woven bone. Shown on the right are TRAP-stained tumor-free and tumor-bearing bone sections. Osteoclasts are stained red, indicated by green arrows. The percentage of bone surface covered by osteoclasts for IgG- and anti-RANKL-treated tumor-bearing femurs were 6.83% and 3.81%, respectively; the percentage of bone surface covered by osteoblasts were 9.01% and 13.04%, respectively.

(D) TGF-β1 amounts in the tumor-bearing bone marrow supernatants of the IgG- and anti-RANKL-treated mice. Data are represented as median ± interquartile range. *p < 0.05, **p < 0.01, ***p < 0.001; ns, not significant. See also Figure S6C.

tumoral CD8 T cells. In total, 2,440, 1,286, 1,005, and 1,558 CD8 T cells from IgG, anti-TGF-β, anti-CTLA-4, and combination-treated tumors were analyzed, respectively. TCR identification showed low clonal enrichment of intra-tumoral CD8 T cells in the IgG- or anti-TGF-β-treated bone CRPC tumors (Figure 6A). Anti-CTLA-4 therapy slightly expanded one clone (TRA: CAMREWDNQGKLIF and TRB: CASSQEGGSAETLYF; 39 cells, 3.88% of total CD8 T cells), and the combination therapy dramatically expanded clone-1 (TRA: CAMREVT and TRB: CSADRGFNSPLYF; 234 cells, 15.02% of total CD8 T cells), making it the dominant clone among the intra-tumoral CD8 T cells (Figures 6A and S7).

We next performed a gene set enrichment analysis (GSEA) on the expression profiles of the expanded clone-1 cells and the cells of the non-expanded clones in the combination-treated tumor via two independent gene sets from a previous publication (the effector and memory CD8 T-cell-associated gene lists) (Tables S2 and S3) (Doering et al., 2012). The genes associated with effector and memory CD8 T cells were strongly enriched in the expanded clone-1 profile (Figure 6B). The clone-1 cells showed high amounts of T-bet and Eomes (Figure 6C), which determine the fate of effector and memory CD8 T cells in a synergistic and partially redundant manner (Intlekofer et al., 2005). The clone-1 cells also expressed high amounts of cytotoxic factors (perforin, granzyme K, and FasL) and T cell activation surface markers (NKG7 and CTLA-2a) (Doering et al., 2012), indicating an activated state. In addition, the expanded clone showed upregulated effector / memory-associated chemokines and receptors (CCL4, CCL5, CCR5, CCR2, and CXCR3) (Doering et al., 2012; Kurachi et al., 2011; Marçais et al.,

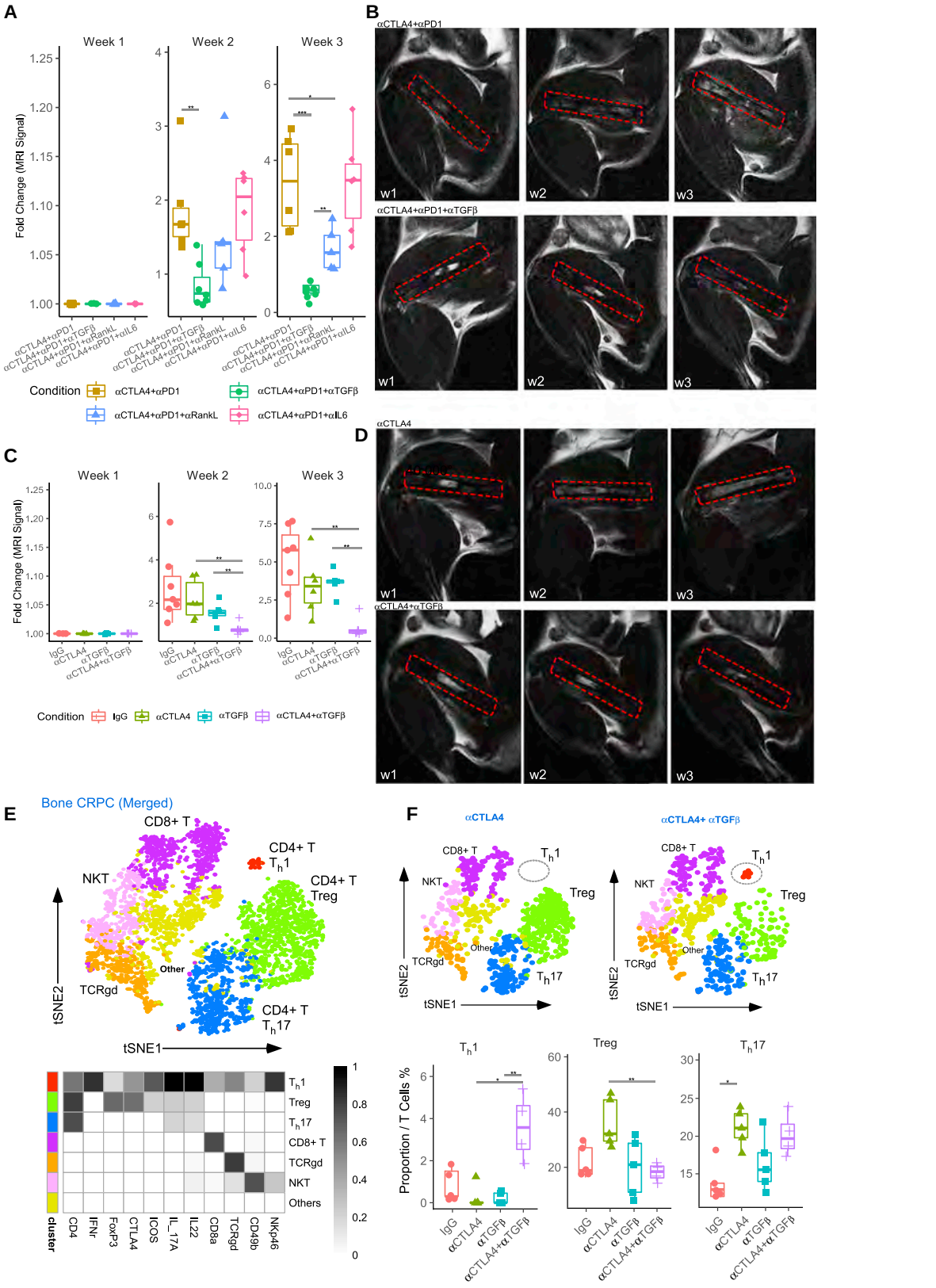

(legend on next page)

2006), as well as the transcriptional factor Runx3 that is essential for the retention of CD8 T cell in tumor tissues (Milner et al., 2017), and the tissue-residency integrin (ITGb1, ITGb2, and ITGa4) (Figure 6C). Altogether, the intra-tumoral expanded clone-1 CD8 T cells were the tumor-resident effector memory T cells. In contrast, the non-expanded clones consisted of phenotypically naive-like bystander T cells, as indicated by high amounts of the homing markers (CD62L and CCR7) and naive-resting T-cell-associated transcriptional factors (TCF7 and LEF1) and low amounts of cytotoxic factors, Runx3, and integrin (Figure 6C).

We next used the Monocle 2 algorithm to determine the pseudo-temporal developmental trajectory of the intra-tumoral CD8 T cells in the combination-treated tumor on the basis of gene expression similarities (Qiu et al., 2017). The intra-tumoral CD8 T cells were first divided into 8 clusters (C0–C7) (Figure 7A): C0 and C3 showed typical naive T cell phenotype (C0/C3-naive); C2 and C7 showed a transition state from naive to effector T cells (C2/C7-naive-effector); C4, C5, and C6 showed effector-like signature (C4–C6-effector-like), and C5 expressed Ki67 (C5- proliferative effector-like); C1 showed memory-effector signature (C1-memory effector) (Figures 7A and 7B). Furthermore, the TCR identification analysis demonstrated that the majority of clone-1 CD8 T cells (n = 234) were located in C1-memory-effector cluster, and the remaining were in C5-proliferative-effector-like cluster, indicating a transition state (Figure 7C). No cells were detected in the naive T cell clusters, consistent with the fact that antigen experience is the pre-requisite for clonal expansion in peripheral tissues. After incorporating the clustering information into the trajectory analysis, we found that the pseudo-temporal ordering began with C0/C3-naive clusters which transitioned into the C2-naive-effector cluster, followed by C4/C6-effector, and terminated with the C1-memory-effector clusters (Figure 7D, top). The clone-1 T cells were highly enriched in the late period of the pseudotime, indicating that the T cells transitioned from antigen recognition to effector and then to memory effector cells (Figure 7D, bottom). Altogether, the tumor-specific CD8 T cells clonally expand after combination therapy, and most cells demonstrate a memory-effector signature.

DISCUSSION

Despite recent advances in second-generation androgen receptor signaling inhibitors, mCRPC that has metastasized to bone remains a largely lethal disease. ICT is a novel therapeutic option for CRPC that has metastasized to bone, although the potential immunological consequences remain unclear. We observed a sub-optimal clinical response to ICT in patients with mCRPC to the bone compared with those with metastases in the soft tissues, which led us to hypothesize that the lack of T_h1 lineage expansion in the bone tumor microenvironment after ICT is a potential resistance mechanism. We established murine models of bone and subcutaneous CRPC to test the efficacy of ICT and evaluate the intra-tumoral immune cell subsets. ICT shows minimal therapeutic effects in bone CRPC, but results in significant regression of subcutaneous CRPC, indicating distinct immunological niches. Although ICT induces CD4 T cell expansion in both subcutaneous and bone CRPC, the lineages are respectively skewed to T_h1 and T_h17. Furthermore, our data indicate that tumor-bearing femurs have significant remodeling and excessive bone resorption, which results in high amounts of active TGF-β within the tumor microenvironment. Combined with the physiologically high amounts of IL-6 in the bone marrow, TGF-β elevation might polarize CD4 T cells to T_h17 cells rather than T_h1 effector cells. Consistent with this, simultaneous blocking of TGF-β might restore T_h1 lineage polarization and promote clonal expansion of intra-tumoral antigen-specific CD8 T cells and subsequent differentiation to anti-tumor memory effector T cells. Of note, our study cannot rule out the possibility that anti-TGF-β treatment might have effects outside the bone marrow metastatic niche. For example, systemic anti-TGF-β administration might also overcome immune suppression that exists in multiple tissues, such as tumor draining lymph node, thereby improving anti-tumor immune responses.

ICT elicits durable clinical responses in a fraction of patients with specific cancer types. Recalcitrance of some tumors to ICT might be because of low amounts of tumor-associated antigens and low frequency of tumor-infiltrating T cells, which is true of prostate cancer, a tumor type with few mutations and few tumor-infiltrating T cells (Ribas and Wolchok, 2018; Samstein et al., 2019). However, as shown in Figure S7, we found that ICT monotherapy increases intra-tumoral CD4 helper T cells with a concomitant increase in a CD8 T cell clone, which suggests that tumors with low mutation burden, such as prostate cancer, might have sufficient amounts of tumor-associated antigens to activate T cells but effective combination therapies might be needed to further drive T cell responses toward anti-tumor immunity. As compared to untreated bone tumors or monotherapy-treated bone tumors, we found that ICT plus anti-TGF-β

Figure 5. TGF-β Blockade Restores T_h1 Lineage Polarization and Augments ICT in Bone CRPC

(A) Fold changes in tumor volume of bone CRPC in mice treated with anti-CTLA-4 + anti-PD-1 + anti-TGF-β or anti-IL-6 or anti-RANKL. *p < 0.05, **p < 0.01, ***p < 0.001; ns, not significant.

(B) Representative MRI scans of tumor-bearing bones in mice treated with anti-CTLA-4 + anti-PD-1 or anti-CTLA-4 + anti-PD-1 + anti-TGF-β.

(C) Fold changes in tumor volume of bone CRPC in mice treated with IgG control antibody or anti-CTLA-4 or anti-TGF-β or anti-CTLA-4 + anti-TGF-β. *p < 0.05, **p < 0.01, ***p < 0.001; ns, not significant.

(D) Representative MRI scans of tumor-bearing bones in mice treated with anti-CTLA-4 or anti-CTLA-4 + anti-TGF-β.

(E) Merged CyTOF profiles of tumor-infiltrating $CD3\varepsilon^+CD11b^-$ T cells of bone CRPC mice treated with IgG control, anti-CTLA-4, anti-TGF-β, and combination. Shown at the top is a tSNE of the annotated T cell lineages, and shown on the bottom is a heatmap of marker expression of each lineage.

(F) At the top is a representative tSNE of tumor-infiltrating T cell lineages in individual anti-CTLA-4- or combination-treated bone CRPC. On the bottom is the proportion of each annotated T_h lineages in bone CRPC of individual mice from each treatment group. Samples for CyTOF analysis were obtained from the mice 3 days after the last dose of a total of 3 doses of therapy. Data are represented as median ± interquartile range. *p < 0.05, **p < 0.01, ***p < 0.001; ns, not significant. See also Figures S6E and S6F illustrating the survival data of the combination therapy.

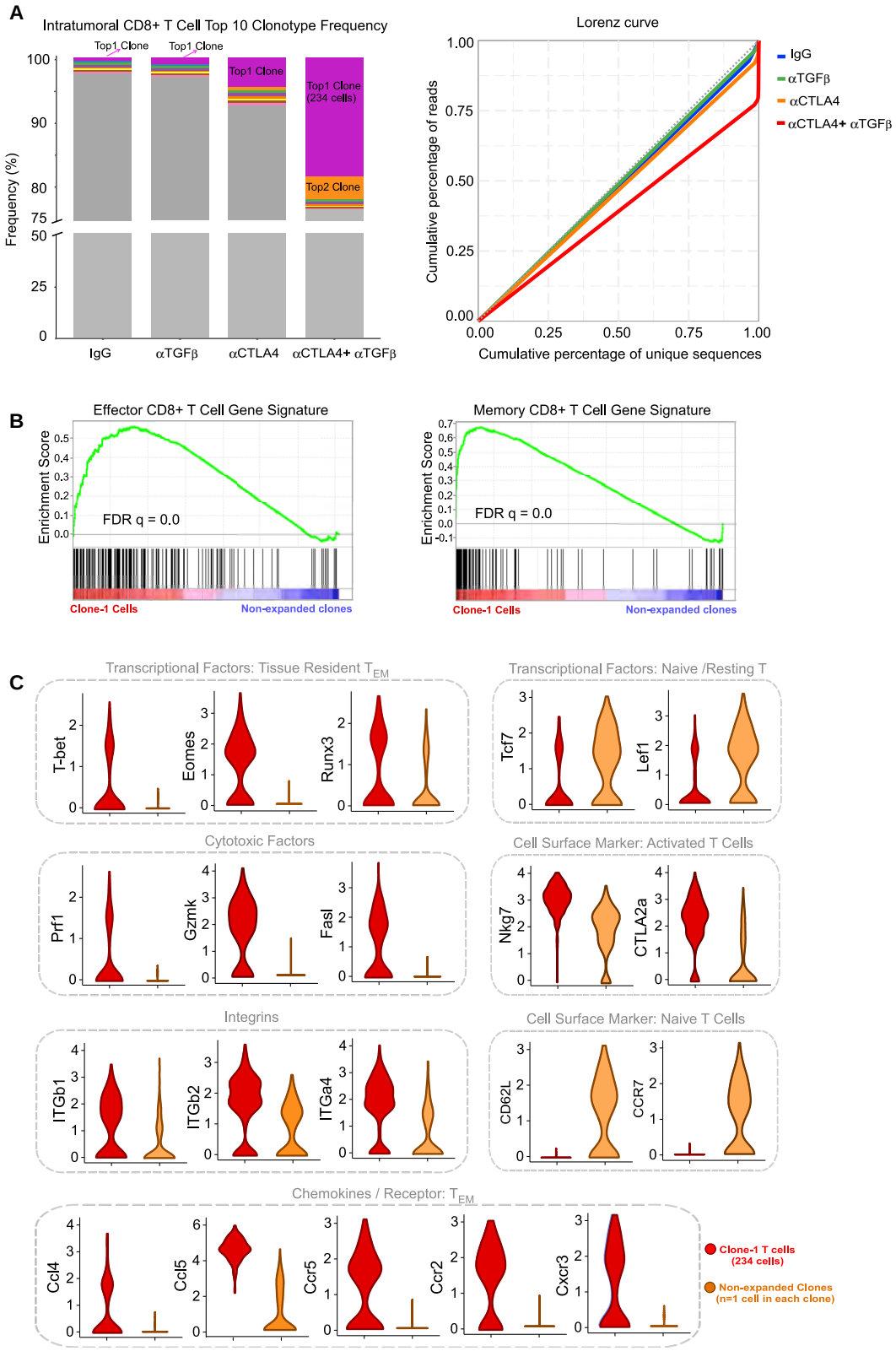

(legend on next page)

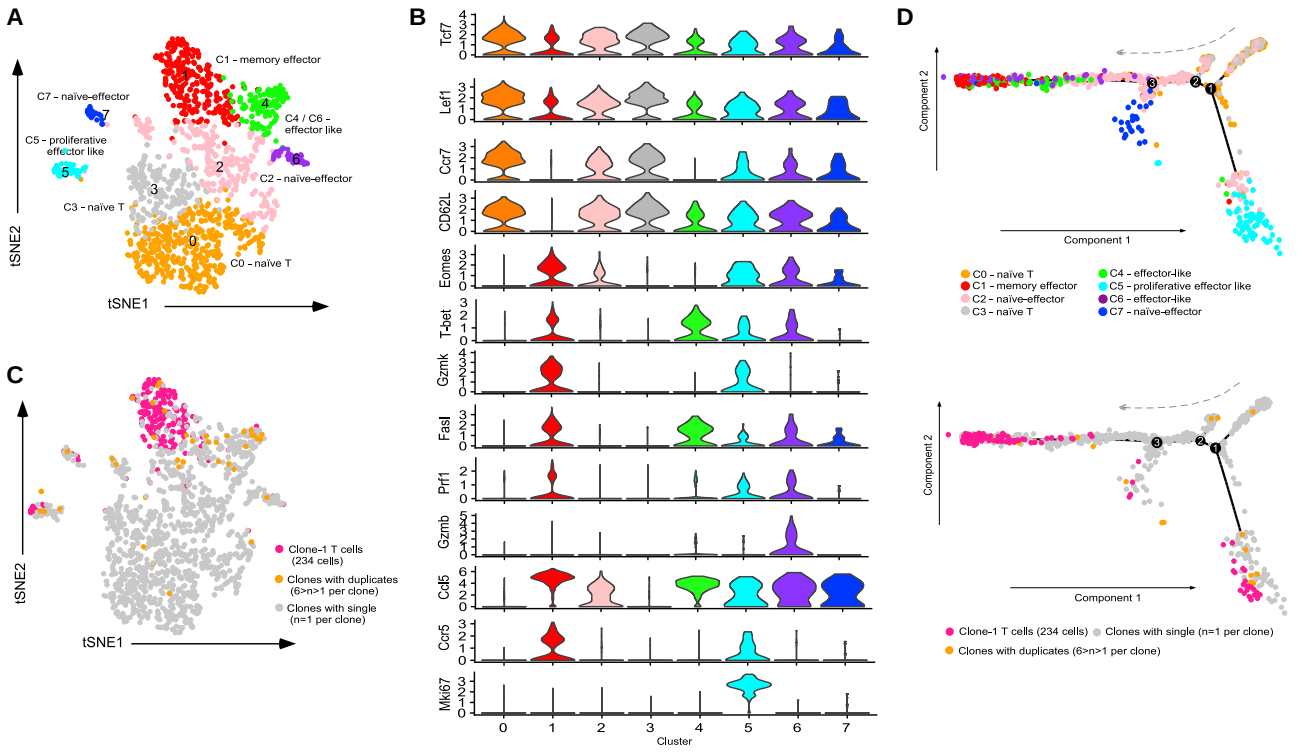

Figure 7. Characteristics of Intra-Tumoral CD8 T Cell Clusters and Clonal Expansion

(A) tSNE plot showing the distribution of 8 clusters of the intra-tumoral CD8 T cells from the bone CRPC mouse treated with αCTLA4 + αTGF-β. Each point represents one cell.

(B) Violin plots showing typical marker expression amounts in each cluster. The numerical characters indicate the cluster number.

(C) The location of clone-1 (234 cells), clone with duplicates (6 > n > 1 cells per clonetype), and non-expanded clone (one cell in each clonotype) on the tSNE plot. Each point represents one cell.

(D) Shown at the top is the pseudo-temporal trajectory of intra-tumoral CD8 T cells in the combination-treated tumor in a two-dimensional space defined by Monocle 2. Each color indicates one cluster and each point represents one cell. The gray arrow indicates the development direction. On the bottom is the same pseudo-time plot as the top. Different colors indicate expanded clone-1 (red), clone represented by one cell (gray), and clone with duplicate cells (6 > n > 1 cells per clonetype) (yellow). Each point represents one cell.

combination therapy increased intra-tumoral CD4 helper T cells, specifically effector T_h1 cells, which elicited significantly higher clonal expansion of the CD8 T cell clone in bone CRPC and led to anti-tumor responses.

Given the dynamic and complex nature of anti-cancer immunity and the existence of multiple immune regulatory receptors and their ligands, it is necessary to supplement ICT with other therapies to optimize its efficacy (Sharma and Allison, 2015). Strategies include creation of an immunogenic microenvironment in a non-immunogenic tumor by using vaccines or radiation or targeting multiple immune co-stimulatory or inhibitory receptors-ligands in a non-redundant fashion (Sharma et al., 2017). Few studies have explored the resistance mechanisms associated with different tissue niches or devised combination strategies tailored specifically to the different tissue niches. The organ-specific niche, such as bone and liver, might be resistant to the development of T_h1 effector CD4 T cells or CD8 cytotoxic T cells, which might explain why ICTs have had limited success in treating patients with liver or bone metastases. Here, for the first time, we provide data that demonstrate the significance of the organ-specific niche in dictating differences in T cell lineages, which play a role in determining response to immune checkpoint therapy. These data have implications for how patients with metastatic

Figure 6. TGF-β Blockade Augments Antigen-Specific Effector / Memory CD8 T Cell Clonal Expansion in Bone CRPC Tumors

(A) Intra-tumoral CD8 T cell TCR diversity was visualized by plotting the cumulative frequency of the top 900 most frequent clones. Each clone containing more than one cell is represented by a unique color and all clones with one cell by gray color. The Lorenz curve for each sample shows IgG- and monotherapy-treated samples near the dotted diagonal line (the line of equality) and a more bowed shape of combination-treated samples.

(B) Comparison of the expression profiles of the expanded clone-1 and non-expanded clones in the combination-treated tumor by GSEA using the effector and memory CD8 T cell gene signature.

(C) Violin plots of a set of known marker genes. The tumor tissues for single-cell sequencing analysis were obtained from the bone CRPC mice 3 days after the last dose of a 3-dose IgG or αCTLA-4 or αTGF-β or anti-CTLA-4 + anti-TGF-β. Abbreviation is as follows: T_{EM}, effector memory T cells. See also Figure S7.

disease are selected for clinical trials as well as indicating the need to select rational combination immunotherapy strategies based on sites of metastases.

Healthy bone structure depends on the balance between osteoblasts and osteoclasts, which is disrupted in pathophysiological conditions like tumor bone metastases. Although prostate cancer bone metastases have been considered pathologically osteoblastic (Logothetis and Lin, 2005), both cells have been implicated—directly or indirectly—in bone metastases (Berish et al., 2018). The osteoclastic activity and bone resorption are significantly enhanced in tumor-bearing bones compared with contralateral healthy bones. The osteolytic process most likely releases a large amount of immobilized TGF-β into the bone matrix. In addition, the bone marrow stromal cells are potential sources of the high physiological amount of IL-6 in the bone marrow, which is essential for the osteoblastic process (Ogasawara et al., 1996). The elevated TGF-β and IL-6 amounts create a distinct cytokine environment seen during metastasis-induced bone remodeling.

The contributions of T_h17 cells to autoimmunity and allergy response are well appreciated (Noack and Miossec, 2014). However, it remains unclear whether T_h17 cells play a role in anti-tumor responses as reviewed by many groups (Asadzadeh et al., 2017; Bailey et al., 2014; Martin et al., 2012; Zou and Restifo, 2010). There are many studies debating whether T_h17 are pro-tumorigenic, anti-tumorigenic, or neutral within the tumor microenvironment (Bronkhorst et al., 2012; Galon et al., 2006; He et al., 2011; Punt et al., 2016; Tosolini et al., 2011; Zhang et al., 2009). In addition, our study is unable to determine an exact role for T_h17 cells in anti-cancer immunity. It is possible that T_h17 is neither stimulatory like Th1 nor suppressive like Treg cells, but rather is an "inert" fraction. Our study also highlights that T_h1 effector cells might fail to develop in bone metastases because of a distinct cytokine microenvironment consisting of TGF-β and IL-6, which might skew T cell development toward T_h17 cells rather than T_h1 effector cells. Our data strongly indicate that T_h1 lineage polarization in the bone tumor microenvironment is essential for the optimal effects of ICT.

In conclusion, resistance mechanisms to ICT in bone metastases include TGF-β-mediated restraining of T_h1 lineage development and inadequate clonal expansion and activation of cytotoxic CD8 T cells, which can be circumvented by simultaneously blocking TGF-β and immune checkpoint receptors.

STAR★METHODS

Detailed methods are provided in the online version of this paper and include the following:

- KEY RESOURCES TABLE
- LEAD CONTACT AND MATERIALS AVAILABILITY
- EXPERIMENTAL MODELS AND SUBJECT DETAILS
  - Clinical trials and human subjects
  - Cell lines
  - Mice
- METHOD DETAILS
  - Bone and subcutaneous castration-resistant prostate cancer (CRPC) mouse models
  - Animal treatment protocol
  - Tumor imaging of bone CRPC mouse models
  - Quantification of murine testosterone levels
  - Collection of bone marrow and soft tissue tumor supernatants
  - Cytokine profiling
  - Cytometry by time of flight (CyTOF) antibody conjugation
  - CyTOF analysis of tumors
  - Library preparation for 10X genomics single-cell 5′ gene expression and V(D)J sequencing
- QUANTIFICATION AND STATISTICAL ANALYSIS
  - Analysis of CyTOF datasets
  - Single-cell RNaseq analysis
  - TCR identification
  - Statistical analysis
- DATA AND CODE AVAILABILITY
  - Data analysis and data availability

SUPPLEMENTAL INFORMATION

Supplemental Information can be found online at https://doi.org/10.1016/j.cell.2019.10.029.

ACKNOWLEDGMENTS

We thank the Immunotherapy Platform at MD Anderson Cancer Center for assistance with the clinical trial samples. We thank Drs. Qing Xiong and Hao Zhao for their bioinformatics input. Dr. Sharma is a member of the Parker Institute for Cancer Immunotherapy and the co-director of the Parker Institute for Cancer Immunotherapy at MD Anderson Cancer Center.

AUTHOR CONTRIBUTIONS

Supervision and Study Oversight, P.S.; Methodology, P.S. and S.J.; Investigation, S.J.; Software, Formal Analysis, and Visualization, P.S., S.J., and Z.G.; Writing, Review, & Editing, P.S., S.J., S.K.S., A.A., and Z.G.; Funding Acquisition, P.S.; Resources, P.S., S.J., S.K.S., A.A., Z.G., B.G., and Y.M.

DECLARATION OF INTERESTS

Dr. Sharma has ownership in Jounce, Neon, Constellation, Oncolytics, BioAtla, Forty-Seven, Apricity, Polaris, Marker Therapeutics, Codiak, ImaginAb, Dragonfly, Lytix, and Hummingbird. Dr. Sharma serves as a consultant for Constellation, Jounce, Neon, BioAtla, Pieris Pharmaceuticals, Oncolytics Biotech, Forty-Seven, Polaris, Apricity, Marker Therapeutics, Codiak, ImaginAb, Dragonfly, Lytix, and Hummingbird. None of the current relationships are related to the study in the manuscript. The other authors declare no competing interests.

Received: April 15, 2019
Revised: July 23, 2019
Accepted: October 23, 2019
Published: November 14, 2019

REFERENCES

Amir el, A.D., Davis, K.L., Tadmor, M.D., Simonds, E.F., Levine, J.H., Bendall, S.C., Shenfeld, D.K., Krishnaswamy, S., Nolan, G.P., and Pe'er, D. (2013). viSNE enables visualization of high dimensional single-cell data and reveals phenotypic heterogeneity of leukemia. Nat Biotechnol *31*, 545–552.

Asadzadeh, Z., Mohammadi, H., Safarzadeh, E., Hemmatzadeh, M., Mahdian-Shakib, A., Jadidi-Niaragh, F., Azizi, G., and Baradaran, B. (2017). The paradox of Th17 cell functions in tumor immunity. Cell. Immunol. *322*, 15–25.

Bailey, S.R., Nelson, M.H., Himes, R.A., Li, Z., Mehrotra, S., and Paulos, C.M. (2014). Th17 cells in cancer: the ultimate identity crisis. Front. Immunol. *5*, 276.

Beer, T.M., Kwon, E.D., Drake, C.G., Fizazi, K., Logothetis, C., Gravis, G., Ganju, V., Polikoff, J., Saad, F., Humanski, P., et al. (2017). Randomized, double-blind, phase III trial of ipilimumab versus placebo in asymptomatic or minimally symptomatic patients with metastatic chemotherapy-naive castration-resistant prostate cancer. J. Clin. Oncol. *35*, 40–47.

Berish, R.B., Ali, A.N., Telmer, P.G., Ronald, J.A., and Leong, H.S. (2018). Translational models of prostate cancer bone metastasis. Nat. Rev. Urol. *15*, 403–421.

Boyce, B.F., and Xing, L. (2008). Functions of RANKL/RANK/OPG in bone modeling and remodeling. Arch. Biochem. Biophys. *473*, 139–146.

Bronkhorst, I.H., Vu, T.H., Jordanova, E.S., Luyten, G.P., Burg, S.H., and Jager, M.J. (2012). Different subsets of tumor-infiltrating lymphocytes correlate with macrophage influx and monosomy 3 in uveal melanoma. Invest. Ophthalmol. Vis. Sci. *53*, 5370–5378.

Chen, H., Liakou, C.I., Kamat, A., Pettaway, C., Ward, J.F., Tang, D.N., Sun, J., Jungbluth, A.A., Troncoso, P., Logothetis, C., and Sharma, P. (2009). Anti-CTLA-4 therapy results in higher CD4+ICOShi T cell frequency and IFN-gamma levels in both nonmalignant and malignant prostate tissues. Proc. Natl. Acad. Sci. USA *106*, 2729–2734.

Chiu, C.P., Moulds, C., Coffman, R.L., Rennick, D., and Lee, F. (1988). Multiple biological activities are expressed by a mouse interleukin 6 cDNA clone isolated from bone marrow stromal cells. Proc. Natl. Acad. Sci. USA *85*, 7099–7103.

Doering, T.A., Crawford, A., Angelosanto, J.M., Paley, M.A., Ziegler, C.G., and Wherry, E.J. (2012). Network analysis reveals centrally connected genes and pathways involved in CD8+ T cell exhaustion versus memory. Immunity *37*, 1130–1144.

Dong, H., Strome, S.E., Salomao, D.R., Tamura, H., Hirano, F., Flies, D.B., Roche, P.C., Lu, J., Zhu, G., Tamada, K., et al. (2002). Tumor-associated B7-H1 promotes T-cell apoptosis: a potential mechanism of immune evasion. Nat. Med. *8*, 793–800.

Fu, S., Zhang, N., Yopp, A.C., Chen, D., Mao, M., Chen, D., Zhang, H., Ding, Y., and Bromberg, J.S. (2004). TGF-beta induces Foxp3 + T-regulatory cells from CD4 + CD25 - precursors. Am. J. Transplant. *4*, 1614–1627.

Fuchs, C.S., Doi, T., Jang, R.W., Muro, K., Satoh, T., Machado, M., Sun, W., Jalal, S.I., Shah, M.A., Metges, J.P., et al. (2018). Safety and efficacy of pembrolizumab monotherapy in patients with previously treated advanced gastric and gastroesophageal junction cancer: phase 2 clinical KEYNOTE-059 trial. JAMA Oncol. *4*, e180013.

Galon, J., Costes, A., Sanchez-Cabo, F., Kirilovsky, A., Mlecnik, B., Lagorce-Pagès, C., Tosolini, M., Camus, M., Berger, A., Wind, P., et al. (2006). Type, density, and location of immune cells within human colorectal tumors predict clinical outcome. Science *313*, 1960–1964.

Gao, J., Ward, J.F., Pettaway, C.A., Shi, L.Z., Subudhi, S.K., Vence, L.M., Zhao, H., Chen, J., Chen, H., Efstathiou, E., et al. (2017). VISTA is an inhibitory immune checkpoint that is increased after ipilimumab therapy in patients with prostate cancer. Nat. Med. *23*, 551–555.

Halabi, S., Kelly, W.K., Ma, H., Zhou, H., Solomon, N.C., Fizazi, K., Tangen, C.M., Rosenthal, M., Petrylak, D.P., Hussain, M., et al. (2016). Meta-analysis evaluating the impact of site of metastasis on overall survival in men with castration-resistant prostate cancer. J. Clin. Oncol. *34*, 1652–1659.

He, S., Fei, M., Wu, Y., Zheng, D., Wan, D., Wang, L., and Li, D. (2011). Distribution and clinical significance of Th17 cells in the tumor microenvironment and peripheral blood of pancreatic cancer patients. Int. J. Mol. Sci. *12*, 7424–7437.

Hellmann, M.D., Rizvi, N.A., Goldman, J.W., Gettinger, S.N., Borghaei, H., Brahmer, J.R., Ready, N.E., Gerber, D.E., Chow, L.Q., Juergens, R.A., et al. (2017). Nivolumab plus ipilimumab as first-line treatment for advanced non-small-cell lung cancer (CheckMate 012): results of an open-label, phase 1, multicohort study. Lancet Oncol. *18*, 31–41.

Hodi, F.S., O'Day, S.J., McDermott, D.F., Weber, R.W., Sosman, J.A., Haanen, J.B., Gonzalez, R., Robert, C., Schadendorf, D., Hassel, J.C., et al. (2010). Improved survival with ipilimumab in patients with metastatic melanoma. N. Engl. J. Med. *363*, 711–723.

Intlekofer, A.M., Takemoto, N., Wherry, E.J., Longworth, S.A., Northrup, J.T., Palanivel, V.R., Mullen, A.C., Gasink, C.R., Kaech, S.M., Miller, J.D., et al. (2005). Effector and memory CD8+ T cell fate coupled by T-bet and eomesodermin. Nat. Immunol. *6*, 1236–1244.

Ishimi, Y., Miyaura, C., Jin, C.H., Akatsu, T., Abe, E., Nakamura, Y., Yamaguchi, A., Yoshiki, S., Matsuda, T., Hirano, T., et al. (1990). IL-6 is produced by osteoblasts and induces bone resorption. J. Immunol. *145*, 3297–3303.

Janssen, E.M., Lemmens, E.E., Wolfe, T., Christen, U., von Herrath, M.G., and Schoenberger, S.P. (2003). CD4+ T cells are required for secondary expansion and memory in CD8+ T lymphocytes. Nature *421*, 852–856.

Kurachi, M., Kurachi, J., Suenaga, F., Tsukui, T., Abe, J., Ueha, S., Tomura, M., Sugihara, K., Takamura, S., Kakimi, K., and Matsushima, K. (2011). Chemokine receptor CXCR3 facilitates CD8(+) T cell differentiation into short-lived effector cells leading to memory degeneration. J. Exp. Med. *208*, 1605–1620.

Larkin, J., Chiarion-Sileni, V., Gonzalez, R., Grob, J.J., Cowey, C.L., Lao, C.D., Schadendorf, D., Dummer, R., Smylie, M., Rutkowski, P., et al. (2015). Combined nivolumab and ipilimumab or monotherapy in untreated melanoma. N. Engl. J. Med. *373*, 23–34.

Leach, D.R., Krummel, M.F., and Allison, J.P. (1996). Enhancement of antitumor immunity by CTLA-4 blockade. Science *271*, 1734–1736.

Liakou, C.I., Kamat, A., Tang, D.N., Chen, H., Sun, J., Troncoso, P., Logothetis, C., and Sharma, P. (2008). CTLA-4 blockade increases IFNgamma-producing CD4+ICOShi cells to shift the ratio of effector to regulatory T cells in cancer patients. Proc. Natl. Acad. Sci. USA *105*, 14987–14992.

Lin, J.T., Martin, S.L., Xia, L., and Gorham, J.D. (2005). TGF-beta 1 uses distinct mechanisms to inhibit IFN-gamma expression in CD4+ T cells at priming and at recall: differential involvement of Stat4 and T-bet. J. Immunol. *174*, 5950–5958.

Logothetis, C.J., and Lin, S.H. (2005). Osteoblasts in prostate cancer metastasis to bone. Nat. Rev. Cancer *5*, 21–28.

Mangan, P.R., Harrington, L.E., O'Quinn, D.B., Helms, W.S., Bullard, D.C., Elson, C.O., Hatton, R.D., Wahl, S.M., Schoeb, T.R., and Weaver, C.T. (2006). Transforming growth factor-beta induces development of the T(H)17 lineage. Nature *441*, 231–234.

Marçais, A., Coupet, C.A., Walzer, T., Tomkowiak, M., Ghittoni, R., and Marvel, J. (2006). Cell-autonomous CCL5 transcription by memory CD8 T cells is regulated by IL-4. J. Immunol. *177*, 4451–4457.

Martin, F., Apetoh, L., and Ghiringhelli, F. (2012). Controversies on the role of Th17 in cancer: a TGF-β-dependent immunosuppressive activity? Trends Mol. Med. *18*, 742–749.

Milner, J.J., Toma, C., Yu, B., Zhang, K., Omilusik, K., Phan, A.T., Wang, D., Getzler, A.J., Nguyen, T., Crotty, S., et al. (2017). Runx3 programs $CD8^+$ T cell residency in non-lymphoid tissues and tumours. Nature *552*, 253–257.

Noack, M., and Miossec, P. (2014). Th17 and regulatory T cell balance in autoimmune and inflammatory diseases. Autoimmun. Rev. *13*, 668–677.

Nowicka, M., Krieg, C., Crowell, H.L., Weber, L.M., Hartmann, F.J., Guglietta, S., Becher, B., Levesque, M.P., and Robinson, M.D. (2017). CyTOF workflow: differential discovery in high-throughput high-dimensional cytometry datasets. F1000Res. *6*, 748.

Ogasawara, H., Tsuji, T., Hirano, D., Aoki, Y., Nakamura, M., and Kodama, H. (1996). Induction of IL-6 production by bone marrow stromal cells on the adhesion of IL-6-dependent hematopoietic cells. J. Cell. Physiol. *169*, 209–216.

Park, I.K., Shultz, L.D., Letterio, J.J., and Gorham, J.D. (2005). TGF-beta1 inhibits T-bet induction by IFN-gamma in murine CD4+ T cells through the protein tyrosine phosphatase Src homology region 2 domain-containing phosphatase-1. J. Immunol. *175*, 5666–5674.

Patel, M.R., Ellerton, J., Infante, J.R., Agrawal, M., Gordon, M., Aljumaily, R., Britten, C.D., Dirix, L., Lee, K.W., Taylor, M., et al. (2018). Avelumab in

metastatic urothelial carcinoma after platinum failure (JAVELIN Solid Tumor): pooled results from two expansion cohorts of an open-label, phase 1 trial. Lancet Oncol. *19*, 51–64.

Punt, S., Dronkers, E.A., Welters, M.J., Goedemans, R., Koljenović, S., Bloemena, E., Snijders, P.J., Gorter, A., van der Burg, S.H., Baatenburg de Jong, R.J., and Jordanova, E.S. (2016). A beneficial tumor microenvironment in oropharyngeal squamous cell carcinoma is characterized by a high T cell and low IL-17(+) cell frequency. Cancer Immunol. Immunother. *65*, 393–403.

Qiu, X., Hill, A., Packer, J., Lin, D., Ma, Y.A., and Trapnell, C. (2017). Single-cell mRNA quantification and differential analysis with Census. Nat. Methods *14*, 309–315.

Ribas, A., and Wolchok, J.D. (2018). Cancer immunotherapy using checkpoint blockade. Science *359*, 1350–1355.

Samstein, R.M., Lee, C.H., Shoushtari, A.N., Hellmann, M.D., Shen, R., Janjigian, Y.Y., Barron, D.A., Zehir, A., Jordan, E.J., Omuro, A., et al. (2019). Tumor mutational load predicts survival after immunotherapy across multiple cancer types. Nat. Genet. *51*, 202–206.

Scheper, W., Kelderman, S., Fanchi, L.F., Linnemann, C., Bendle, G., de Rooij, M.A.J., Hirt, C., Mezzadra, R., Slagter, M., Dijkstra, K., et al. (2019). Low and variable tumor reactivity of the intratumoral TCR repertoire in human cancers. Nat. Med. *25*, 89–94.

Schneider, C.A., Rasband, W.S., and Eliceiri, K.W. (2012). NIH Image to ImageJ: 25 years of image analysis. Nat. Methods. *9*, 671–675.

Sharma, P., and Allison, J.P. (2015). The future of immune checkpoint therapy. Science *348*, 56–61.

Sharma, P., Hu-Lieskovan, S., Wargo, J.A., and Ribas, A. (2017). Primary, adaptive, and acquired resistance to cancer immunotherapy. Cell *168*, 707–723.

Sharma, P., Pachynski, R.K., Narayan, V., Flechon, A., Gravis, G., Galsky, M.D., Mahammedi, H., Patnaik, A., Subudhi, S.K., Ciprotti, M., et al. (2019). Initial results from a phase II study of nivolumab (NIVO) plus ipilimumab (IPI) for the treatment of metastatic castration-resistant prostate cancer (mCRPC; CheckMate 650). J. Clin. Oncol. *37*, 142, 142.

Shull, M.M., Ormsby, I., Kier, A.B., Pawlowski, S., Diebold, R.J., Yin, M., Allen, R., Sidman, C., Proetzel, G., Calvin, D., et al. (1992). Targeted disruption of the mouse transforming growth factor-beta 1 gene results in multifocal inflammatory disease. Nature *359*, 693–699.

Siegel, R., Naishadham, D., and Jemal, A. (2012). Cancer statistics, 2012. CA Cancer J. Clin. *62*, 10–29.

Simoni, Y., Becht, E., Fehlings, M., Loh, C.Y., Koo, S.L., Teng, K.W.W., Yeong, J.P.S., Nahar, R., Zhang, T., Kared, H., et al. (2018). Bystander $CD8^+$ T cells are abundant and phenotypically distinct in human tumour infiltrates. Nature *557*, 575–579.

Tosolini, M., Kirilovsky, A., Mlecnik, B., Fredriksen, T., Mauger, S., Bindea, G., Berger, A., Bruneval, P., Fridman, W.H., Pagès, F., and Galon, J. (2011). Clinical impact of different classes of infiltrating T cytotoxic and helper cells (Th1, th2, treg, th17) in patients with colorectal cancer. Cancer Res. *71*, 1263–1271.

Veldhoen, M., Hocking, R.J., Atkins, C.J., Locksley, R.M., and Stockinger, B. (2006). TGFbeta in the context of an inflammatory cytokine milieu supports de novo differentiation of IL-17-producing T cells. Immunity *24*, 179–189.

Wei, S.C., Levine, J.H., Cogdill, A.P., Zhao, Y., Anang, N.A.S., Andrews, M.C., Sharma, P., Wang, J., Wargo, J.A., Pe'er, D., et al. (2017). Distinct cellular mechanisms underlie anti-CTLA-4 and anti-PD-1 checkpoint blockade. Cell *170*, 1120–1133.

Wolchok, J.D., Chiarion-Sileni, V., Gonzalez, R., Rutkowski, P., Grob, J.J., Cowey, C.L., Lao, C.D., Wagstaff, J., Schadendorf, D., Ferrucci, P.F., et al. (2017). Overall survival with combined nivolumab and ipilimumab in advanced melanoma. N. Engl. J. Med. *377*, 1345–1356.

Zhang, J.P., Yan, J., Xu, J., Pang, X.H., Chen, M.S., Li, L., Wu, C., Li, S.P., and Zheng, L. (2009). Increased intratumoral IL-17-producing cells correlate with poor survival in hepatocellular carcinoma patients. J. Hepatol. *50*, 980–989.

Zou, W., and Restifo, N.P. (2010). T(H)17 cells in tumour immunity and immunotherapy. Nat. Rev. Immunol. *10*, 248–256.

STAR★METHODS

KEY RESOURCES TABLE

REAGENT or RESOURCE	SOURCE	IDENTIFIER
Antibodies		
Anti-mouse CD45 (clone 30-F11)	Fluidigm	Cat#3089005B; RRID: AB_2651152
Anti-mouse Ly6G (clone 1A8)	Fluidigm	Cat#3141008B; RRID: AB_1089180
Anti-mouse CD80/86 (clone 16-10A1/ GL1)	Biolegend	Cat#04710; RRID: AB_313131
Anti-mouse CD11c (clone N418)	Fluidigm	Cat#3142003B; RRID: AB_2814737
Anti-mouse TNFα (clone MP6-XT22)	Biolegend	Cat#506310; RRID: AB_10900823
Anti-mouse IL-2 (clone JES6-5H4)	Biolegend	Cat#503812; RRID: AB_315306
Anti-mouse PD-L1 (clone 10F.9G2)	Biolegend	Cat#124302; RRID: AB_961228
Anti-mouse IFNγ (clone XMG1.2)	Biolegend	Cat#505802; RRID: AB_315396
Anti-mouse CD11b (clone M1/70)	Fluidigm	Cat#3148003B; RRID: AB_2814738
Anti-mouse CD19 (clone 6D5)	Fluidigm	Cat#3149002B; RRID: AB_2814679
Anti-mouse IL-6 (clone MP5-20F3)	Biolegend	Cat#504506; RRID: AB_315340
Anti-mouse IL-10 (clone JES5-16E3)	Biolegend	Cat#505012; RRID: AB_389224
Anti-mouse CD3ξ (clone 145-2c11)	Biolegend	Cat#100302; RRID: AB_312667
Anti-mouse PD-1 (clone RMP1-14)	Biolegend	Cat#114102; RRID: AB_313573
Anti-mouse CSF1R (clone AFS98)	Biolegend	Cat#135504; RRID: AB_1937291
Anti-mouse ICOS (clone 7E.17G9)	Biolegend	Cat#117408; RRID: AB_2122603
Anti-mouse CTLA-4 (clone UC10-4B9)	Biolegend	Cat#106302; RRID: AB_313251
Anti-mouse Foxp3 (clone FJK16s)	Fluidigm	Cat#3158003A; RRID: AB_2814740
Anti-mouse CD38 (clone 90)	Biolegend	Cat#102702; RRID: AB_312923
Anti-mouse IL-4 (clone 11B11)	Biolegend	Cat#504102; RRID: AB_315316
Anti-mouse BTLA (clone 6A6)	Biolegend	Cat#139104; RRID: AB_10613110
Anti-mouse IL-22 (clone BL35175)	Biolegend	Cat#517502; RRID: AB_10694243
Anti-mouse CD4 (clone RM4-5)	Biolegend	Cat#100506; RRID: AB_312709
Anti-mouse IL-17A (clone TC11-18H10.1)	Biolegend	Cat#506906; RRID: AB_528927
Anti-mouse SiglecF (clone 1RNM44N)	ThermoFisher	Cat#14-1702-82; RRID: AB_2572866
Anti-mouse TGFβ1 (clone TW7-16B4)	Biolegend	Cat#141402; RRID: AB_10719836
Anti-mouse Ly6C (clone HK1.4)	Biolegend	Cat#128002; RRID: AB_1134214
Anti-mouse CD8a (clone 53-6.7)	Fluidigm	Cat#100716; RRID: AB_312755
Anti-mouse IL-5 (clone TRFK5)	Biolegend	Cat#504302; RRID: AB_315326
Anti-mouse CD49b (clone HMa2)	Fluidigm	Cat#3170008B; RRID: AB_2814741
Anti-mouse TCRγδ (clone GL3)	Biolegend	Cat#118114; RRID: AB_1134229
Anti-mouse FceR1a (clone 1F2A9)	ThermoFisher	Cat#MA5-17074; RRID: AB_2538545
Anti-mouse B220 (clone RA3-6B2)	Biolegend	Cat#103216; RRID: AB_312999
Anti-mouse IL-21 (clone 7H20-I19-M3)	Biolegend	Cat#514302; RRID: AB_1227666
Anti-mouse NKp46 (clone 29A1.4)	Biolegend	Cat#137614; RRID: AB_11124341
Anti-mouse F4/80 (clone BM8)	Biolegend	Cat#123102; RRID: AB_893506
Anti-mouse MHCII (clone M5/114.15.2)	Biolegend	Cat#107610; RRID: AB_313325
Anti-Human CD45 (clone HI30)	Fluidigm	Cat#3089003; RRID: AB_2661851
Anti-Human CD3 (clone UCHT1)	Fluidigm	Cat#300437; RRID: AB_11147760
Anti-Human CD8a (clone RPA-T8)	Biolegend	Cat#301053; RRID: AB_2562810
Anti-Human CD4 (clone RPA-T4)	Biolegend	Cat#300502; RRID: AB_314070
Anti-Human CD56 (clone NCAM16.2)	Fluidigm	Cat#3176008; RRID: AB_2661813

(*Continued on next page*)

Continued

REAGENT or RESOURCE	SOURCE	IDENTIFIER
Anti-Human Tbet (clone 4B10)	Biolegend	Cat#644825; RRID: AB_2563788
Anti-Human TCRγδ (clone 11F2)	Fluidigm	Cat#3152008B; RRID: AB_2687643
Anti-Human RORγt (clone 600214)	R&D	Cat#MAB6109; RRID: AB_10642312
Anti- Human Foxp3 (clone PCH101)	Fluidigm	Cat#3162011; RRID: AB_267650
Anti-TGFβ (clone 1D11)	Bio X cell	Cat#BE0057; RRID: AB_1107757
Anti-CTLA-4 (clone 9H10)	Bio X cell	Cat#BE0131; RRID: AB_10950184
Anti-PD-1 (clone RMP1-14)	Bio X cell	Cat#BE0146; RRID: AB_10949053
Anti-RANKL (clone IK22/5)	Bio X cell	Cat#BE0191; RRID: AB_10949003
Anti-IL-6 (clone MP5-20F3)	Bio X cell	Cat#BE0046; RRID: AB_1107709
Biological Samples		
Human bone marrow biopsies	MDACC; see Table S1	N/A
Chemicals, Peptides, and Recombinant Proteins		
Cell-ID Cisplatin	Fluidigm	Cat#201064
Cell-ID Intercalator Ir	Fluidigm	Cat#201192B
Antibody Stabilizer	Candor Biosciences	Cat#131050
EQ 4-element beads	Fluidigm	Cat#201078
TCEP	Sigma-Aldrich	Cat#77720
16% PFA	EMS	Cat#15710
Degarelix	MDACC Pharmacy	FIRMAGON
Critical Commercial Assays		
X8 Antibody Labeling Kit	Fluidigm	N/A (metal specific)
20-Plex Pd Barcoding Kit	Fluidigm	Cat#201060
Chromium Single Cell 5′ Library Kit	10X Genomics	Cat#PN-1000002
Chromium Single Cell V(D)J Enrichment Kit	10X Genomics	Cat#PN-10000071
Chromium Single Cell 5′ Library Construction Kit	10X Genomics	Cat#PN-1000020
Chromium Chip A Single Cell Kit	10X Genomics	Cat#PN-120236
Chromium i7 Multiplex Kit	10X Genomics	Cat#PN-120262
LEGENDplex multi-analyte flow assay kit	Biolegend	CST-071118-JI-UTMACC
LEGENDplex™ Mouse Free Active/Total TGF-β1 Assay	Biolegend	Cat#740489
U-PLEX TGF-β Combo Human	Meso Scale Diagnostics	Cat#K15241K-4
Tumor Dissociation Kit, Mouse	Miltenyi Biotec	Cat#130-096-730
Testosterone ELISA Kit	Enzo Life Sciences	Cat#ADI-900-065
Qubit dsDNA HS assay kit	Thermo	Cat#Q32851
Agilent 2100 BioAnalyzer High Sensitivity DNA kit	Agilent Technologies	Cat#5067-4626
Deposited Data		
Single-cell RNA sequencing of murine tumor infiltrating T cells	This paper	Sequence Read Archive (SRA): PRJNA577120
Single-cell TCR sequencing of murine tumor infiltrating T cells	This paper	Sequence Read Archive (SRA): PRJNA577120
CyTOF datasets	This paper	Flow Repository: FR-FCM-Z2AH, FR-FCM-Z2AJ, FR-FCM-Z2AX, FR-FCM-Z2AL and FR-FCM-Z2AP
Experimental Models: Cell Lines		
Myc-Cap cell line	ATCC	Cat#CRL-3255
Experimental Models: Organisms/Strains		
FVB/NJ	The Jackson Lab	Cat#001800

(*Continued on next page*)

Continued

REAGENT or RESOURCE	SOURCE	IDENTIFIER
Software and Algorithms		
FlowJo 10.0.8	FlowJo LLC	Version: 10
Prism 7	GraphPad	Version: 7
R software	CRAN	Version: 3.5.1
ImageJ	Schneider et al., 2012	https://imagej.nih.gov/ij/
MATLAB R2015b	Mathworks	Version: R2015b
Cyt	Amir el et al., 2013	Version: Cyt 2
Helios software 6.7	Fluidigm	Version: 6.7
cytofWorkflow	Bioconductor	Version: 1.4.0
Cellranger	https://www.10xgenomics.com	Version: 2.0.0
Seurat	https://satijalab.org/seurat/	Version: 2.3.4
Monocle2	http://cole-trapnell-lab.github.io/monocle-release/	Version: 2.10.0
LymphoSeq	Bioconductor	Version: 1.10.0

LEAD CONTACT AND MATERIALS AVAILABILITY

All materials are publicly available. Further information and requests for resources and reagents should be directed to and will be fulfilled by the Lead Contact, Padmanee Sharma (Padsharma@mdanderson.org).

EXPERIMENTAL MODELS AND SUBJECT DETAILS

Clinical trials and human subjects

Primary prostate tumors were collected and analyzed after patients provided informed consent and received treatment with ipilimumab (anti-CTLA-4) on MDACC IRB-approved protocols PA13-0291 and 2009-0135 as previously published (Gao et al., 2017).

Bone marrow samples from patients with castration-resistant bone-metastatic disease were collected after patients provided informed consent on MDACC IRB-approved protocol PA13-0291. Patients received treatment with ipilimumab on protocols 2014-0386 (NCT02703623) and CA209-650 (NCT02985957).

Cell lines

The murine prostate cancer cell line Myc-CaP (ATCC, CRL-3255) was grown in high-glucose Dulbecco's modified Eagle's medium (DMEM) supplemented with 10% fetal bovine serum (FBS) and penicillin-streptomycin (50 U/mL).It had been independently validated using short tandem repeat DNA fingerprinting at the University of Texas MD Anderson Cancer Center.

Mice

FVB/NJ were obtained from The Jackson Laboratory (Bar Harbor, ME). Male mice were used at 6 weeks of age. All animal experiments were conducted according to the guidelines approved by the MD Anderson Institutional Animal Care and Use Committee.

METHOD DETAILS

Bone and subcutaneous castration-resistant prostate cancer (CRPC) mouse models

The bone metastasis model was established by inoculating tumor cells directly into the bone of male FVB/NJ mice. Briefly, the mice were anesthetized with isoflurane, and after depilating and surface sterilizing the right leg, a 30-gauge needle was carefully inserted with slight drilling under the patella through the middle of the patellar ligament into the anterior intercondylar area on top of the femur. Following successful penetration, 5 μL of Myc-CaP cell suspension (1×10^6 cells) was slowly injected into the bone. The needle was then extracted and the leg sutured, and the animals were given suitable postsurgical care. To induce subcutaneous prostate tumors, the male FVB/NJ mice were injected with the 2×10^6 Myc-CaP cells. Once the tumors reached the size of 150 - 200 mm^3, the mice were subcutaneously injected with 50 mg/kg degarelix, followed by a maintenance dose of 25 mg/kg every 4 weeks to induce tumor regression. The relapse of the regressed tumors indicated the establishment of subcutaneous CRPC.

Animal treatment protocol

The subcutaneous CRPC-bearing mice were injected intra-peritoneally with anti-CTLA-4 (clone 9H10; starting dose 8 mg/kg followed by three doses each of 4 mg/kg) and anti-PD-1 (RMP1-14; 6 mg/kg) antibodies every 3 days for a total of four times. In the

bone-metastasis model, the degarelix regimen was started 4 days after tumor-cell inoculation. Ten days after inoculation, the mice were randomized into 4 treatment groups and appropriately injected with anti-CTLA-4 and anti-PD-1 antibodies (as described above) with or without anti-TGF-β (1D11; 10 mg/kg), anti-interleukin-6 (MP5-20F3; 8 mg/kg) or anti-RANKL (IK22/5; 8 mg/kg) antibodies every 3 days for a total of four times. The first dose was injected intravenously, followed by three intraperitoneal injections.

Tumor imaging of bone CRPC mouse models

Tumors in the bone were visualized using a BioSpec 7T magnetic resonance imaging system (Bruker BioSpin, Billerica, MA), and the tumor volume was evaluated using the ImageJ program (National Institutes of Health, Bethesda, MD). An MX-20 cabinet X-ray system (Faxitron Bioptics, Tucson, AZ) was also used to evaluate tumor volume and bone remodeling.

Quantification of murine testosterone levels

After collection of the whole blood via facial vein, allow the blood to clot for 15 min at room temperature. Remove the clot by centrifuging at 2,000 g for 5 min in a refrigerated centrifuge. The supernatant (serum) can be used to downstream analysis. The serum testosterone level was quantified using an ELISA kit (ADI-900-065; Enzo Life Sciences, Farmingdale, NY) as per the instructions.

Collection of bone marrow and soft tissue tumor supernatants

To obtain murine bone marrow supernatant, the condyles, patella and epiphyses of the tumor-bearing or tumor-free femurs were first removed to expose the metaphysis. The extracted femurs were then placed in 0.5 mL micro centrifuge tubes with a hole in the bottom that were then nested in 1.5 mL tubes. The latter were centrifuged at 10,000 x g for 5 min and the supernatant was collected. The soft tissue tumor supernatants were harvested from the mice by mincing the subcutaneous tumor tissues into 2 mm^3 pieces in a 1.5 mL tube, and centrifuging at 10,000 x g for 5 min. Finally, the bone marrow biopsies from patients were centrifuged at 10,000 × g for 15 min and the supernatants were collected.

Cytokine profiling

The cytokine levels in the murine bone marrow supernatant and serum were profiled using customized LEGENDplex multi-analyte flow assay kit (CST-071118-JI-UTMACC, Refereed to #740489, #740005 and #740134; BioLegend, San Diego, CA) according to the manufacturer's instructions. The TGFβ levels in the human bone marrow supernatants were measured with U-PLEX TGF-β Combo Human (#K15241K-4; Meso Scale Diagnostics, Rockville, MD)

Cytometry by time of flight (CyTOF) antibody conjugation

The antibodies were labeled using the X8 antibody labeling kit as per the manufacturer's protocol (Fluidigm). Briefly, the polymer was dissolved in 95μl L-Buffer provided in the kit, mixed with 5μl lanthanide solution, and incubated for 30 min at 37°C. The lanthanide-loaded polymer solution was transferred to a 3 kDa spin filter column (#OD003C35, Pall Nanosep) and washed with C-Buffer, and re-suspended in 95μl C-Buffer. The unlabeled antibody (100μg) was washed in R buffer on a 50 kDa spin filter column (#UFC505096, Millipore), and reduced in 4mM TCEP (Sigma-Aldrich) in R buffer for 30 min at 37°C. After another wash, the reduced antibody was mixed with lanthanide-loaded polymer in 50 kDa spin filter column and incubated for 60 min at 37°C. The antibody was then washed 4 times with W-buffer, and re-suspended at the concentration of 0.5 mg/mL in antibody stabilizer.

CyTOF analysis of tumors

The tumor tissues were minced and dissociated using a tissue dissociation kit (#130-096-730; Miltenyi Biotec, Bergisch Gladbach, Germany). Single-cell suspensions (3×10^6/mL) were incubated with the antibody cocktail in 100 μL staining buffer (PBS with 5% FBS) at 4°C for 30 min, followed by 2.5μM monoisotopic cisplatin-194Pt (Fluidigm) at room temperature for 1 min. After washing with PBS, the cells were fixed and permeabilized with FOXP3 Fix/Perm buffer (eBioscience, San Diego, CA) for 30 min at room temperature, washed again, and then incubated with an intracellular antibody cocktail for 30 min at 4°C. The cells were washed and barcoded with palladium metal barcoding reagents (Fluidigm) for 30 min at room temperature, rinsed, and incubated overnight in 1.6% paraformaldehyde (in PBS) containing 30nM iridium nucleic acid intercalator (Fluidigm). After another wash with 0.5% bovine serum albumin (BSA) in PBS, the cells were filtered, washed twice with 0.1% BSA, and run in a Helios mass cytometer (Fluidigm). The mass cytometry data were normalized to Equation 4-element calibration bead signal (# 201078, Fluidigm) in 100 s interval windows using normalization software version 2 (Fluidigm). Mass tag barcodes were resolved with a doublet filtering scheme using Debarcoder (Fluidigm).

Library preparation for 10X genomics single-cell 5′ gene expression and V(D)J sequencing

Single RNA-seq and V(D)J libraries were generated using the 10X Genomics Chromium Controller Instrument and Chromium single cell 5′ library & gel bead kit, along with the V(D)J enrichment kit according to manufacturers' instructions. Briefly, 8000 FACS-sorted intra-tumoral T cells (> 92% viability) were loaded on the controller to generate single-cell Gel Bead-In-Emulsions (GEMs). Reverse transcription and sample indexing were used to generate barcoded-cDNA, followed by purification with DynaBeads and PCR-amplification. The amplified barcoded cDNA was used to construct 5′ gene expression libraries and TCR enriched libraries. For 5′ library construction, the amplified cDNA was fragmented, end repaired, A-tailed, sample indexed and double-sized selected with SPRI

beads (average size, 450bp). For the V(D)J library, mouse T cell V(D)J sequences were enriched from the amplified cDNA followed by fragmentation, end repairing, A-tailing, sample indexing and double-sized selection with SPRI beads (average size, 600bp). The DNA quantification and fragment size distribution of the libraries were determined with Qubit dsDNA HS assay kit (Thermo, Q32851) and Agilent 2100 BioAnalyzer High Sensitivity DNA kit (5067-4626). Pooled libraries were then sequenced on an Illumina high-output sequencing platform, with 26bp on the first read and 98bp on the second read for gene expression analysis, and 150bp on the two reads for V(D)J libraries.

QUANTIFICATION AND STATISTICAL ANALYSIS

Analysis of CyTOF datasets

Sample data was manually gated by non-bead, event length, live/dead discrimination in FlowJo, and by the specific surface markers (e.g., CD45, CD3ε, CD11b) for each analysis. The exported .fcs files were then loaded into R for downstream analysis by CyTOF workflow (Nowicka et al., 2017) and Cyt (Amir el et al., 2013). Briefly, data were transformed by arcsinh using a coefficient of 5. Cell populations were identified using either FlowSOM or PhenoGraph. Dimension reduction visualization was carried out using the t-SNE algorithm. For marker expression visualization in heatmaps, the transformed expression values were further normalized between 0 and 1 and the median value of each marker in each cluster were plotted.

Single-cell RNaseq analysis

Single cell gene expression sequencing data were processed through the Cell ranger pipeline (v2.0.0) from the 10X Genomics with default parameters. Briefly, the reads were aligned to the UCSC mm10 transcriptome and the UMI matrices were obtained for each sample. Raw read count tables were analyzed using the Seurat (v2.3.4) pipeline. For each sample, genes that were expressed in less than 3 cells, cells that expressed < 200 genes or > 5000 genes, and cells with mitochondrial genes constituting > 5% were discarded. Highly variable genes were identified using the FindVariableGenes function, and used for PCA analysis. Clusters were identified using the SNN algorithm with a resolution parameter 0.6. Monocle2 (v2.10.0) was used for trajectory analysis of the CD8+ T cell population. Briefly, a CellDataSet object was created with cluster-specific genes and negative binomial as the model of data distribution. The CD8+ T cell trajectory was then inferred by dimension reduction using DDRTree, followed by ordering of the cells. Preranked Gene Set Enrichment Analysis (GSEA) was carried out for the comparison between clonotypes using GSEA Java GUI (v2.3.3). Gene ranking was done by the log2 fold change between two groups under comparison (clone-1 cells versus non-expanded clones). Gene sets were curate based on previous publication (Doering et al., 2012) (Tables S2 and S3).

TCR identification

TCR sequencing data was processed through the Cellranger pipeline (v2.0.0) from the 10X Genomics with default parameters. Antigen receptor repertoire diversity quantified by the number of unique clonotypes were identified and visualized by the barplot and Lorenz Curve using the LymphoSeq (v1.10.0) package.

Statistical analysis

Wilcoxon rank-sum test was used to test statistical significance between two variables: Figures 2B, 2D, 3E, 4A, 4B, 4D, 5A, 5C, 5F, S3C, S5A-S5D, S6C, and S6D. Wilcoxon rank-sum test significant level is defined as $p < 0.05$ (*), $p < 0.01$ (**), $p < 0.001$ (***), and $p > 0.05$ (ns). The Log-rank test was used to determine statistical significance between two or more Kaplan-Meier survival curves, Figures 2C, S3B, S6E, and S6F. All statistical analyses were carried out using R and GraphPad Prism 7 software. P values lower than 0.05 were considered statistically significant.

DATA AND CODE AVAILABILITY

Data analysis and data availability

Data analysis, visualization, and statistical tests were conducted in R (v3.4.4; R foundation for Statistical Computing, Vienna, Austria), Prism 7 (v7, GraphPad Software, San Diego, CA, USA). CyTOF data were deposited to FlowRepository and the Repository IDs are FR-FCM-Z2AH, FR-FCM-Z2AJ, FR-FCM-Z2AX, FR-FCM-Z2AL and FR-FCM-Z2AP. Single cell RNaseq and TCRseq data were deposited in the Sequence Read Archive (SRA) with accession number PRJNA577120. All customized code is available from the corresponding author upon reasonable request.

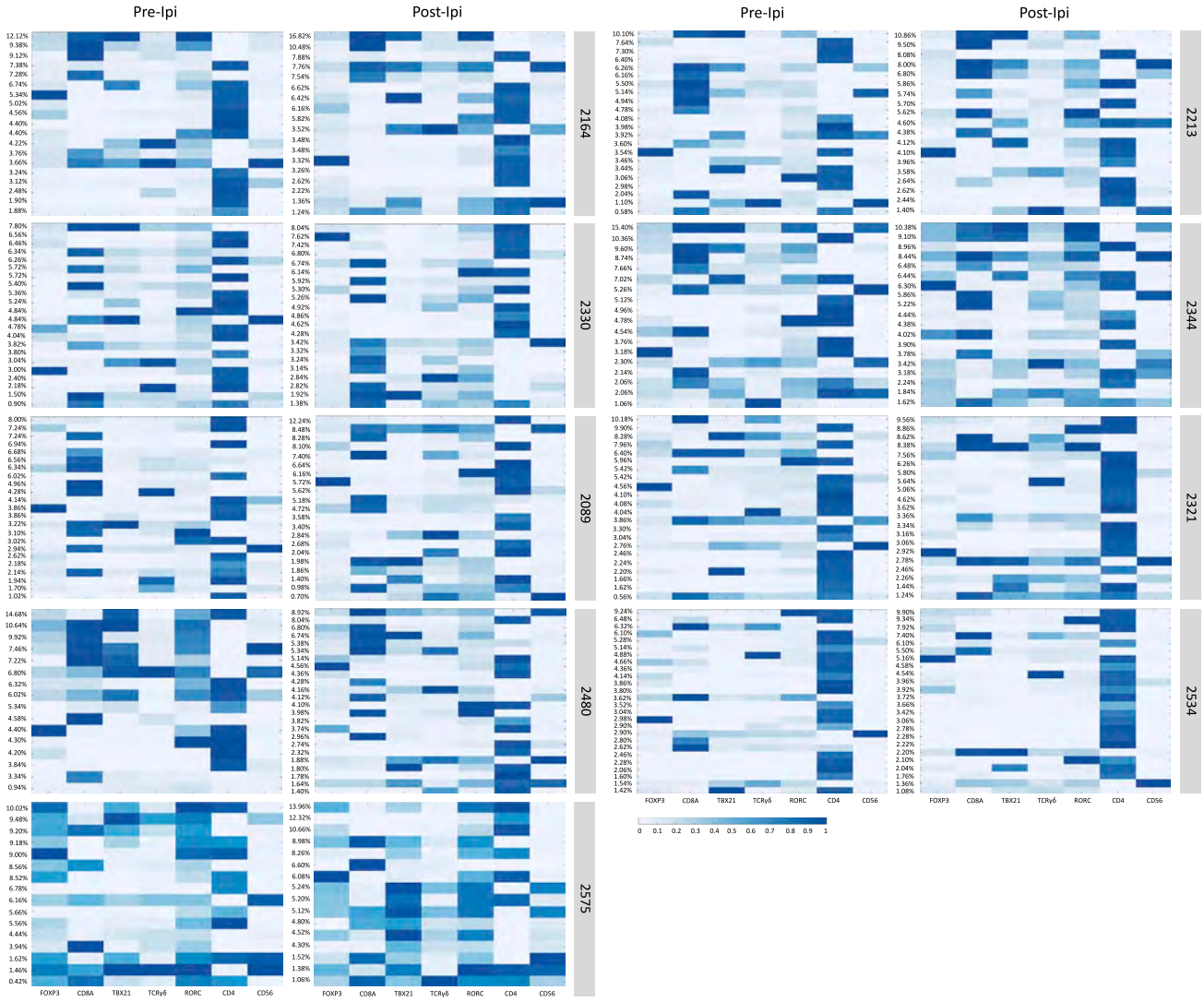

Figure S1. Ipilimumab Induces T_h17 as Opposed to T_h1 Lineage Expansion in Bone Metastases from Patients with Prostate Cancer, Related to Figure 1

Heatmaps showing the immuno-phenotype of each subset of each sample (pre- or post- ipilimumab treated) of 9 patients from two clinical trials (NCT02703623; 02985957).

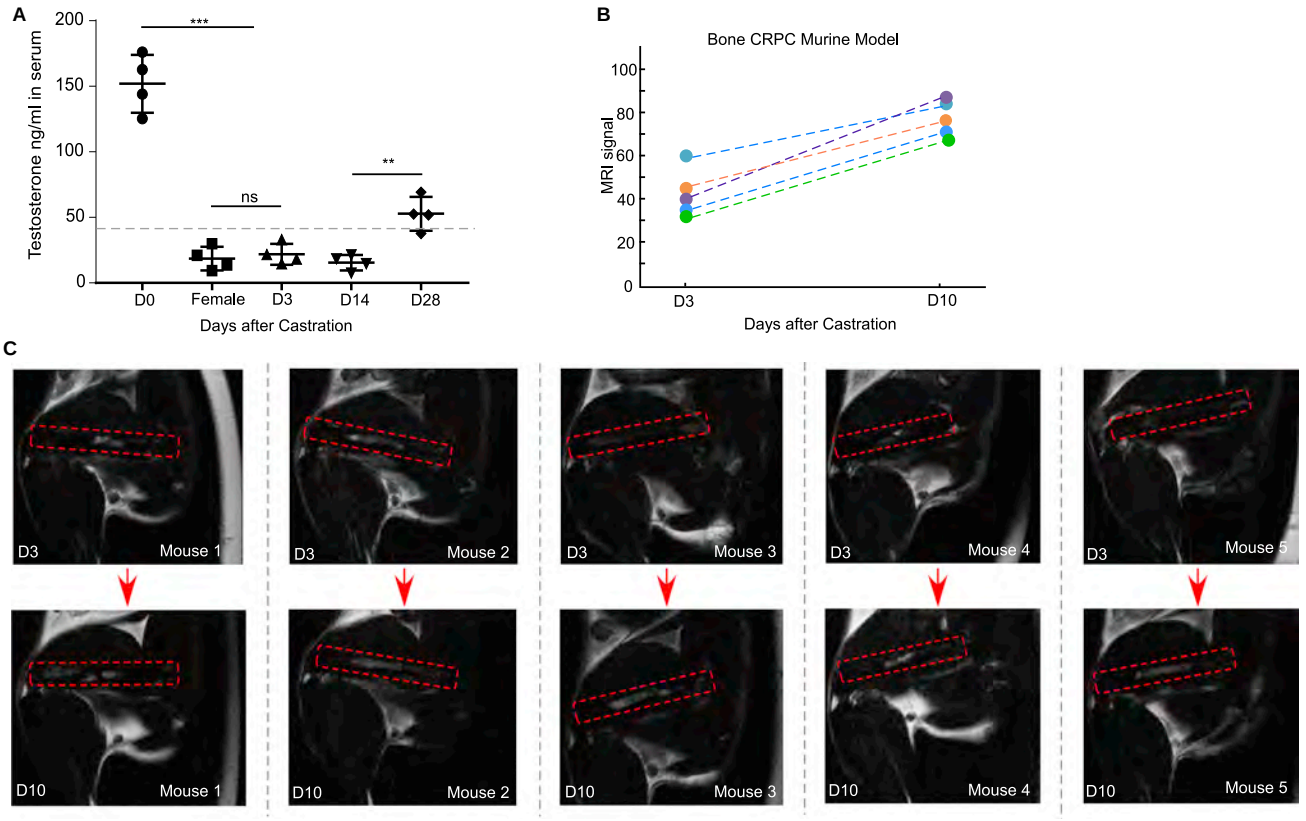

Figure S2. The Establishment of Murine Bone CRPC Model, Related to Figure 2

(A) Quantification of testosterone levels in the sera of degarelix-administered mice. Data are presented as mean ± SEM.

(B) Bone metastatic prostate cancer progression in the castrated state.

(C) Representative MRI scans of tumor-bearing femurs of the chemically castrated mice.

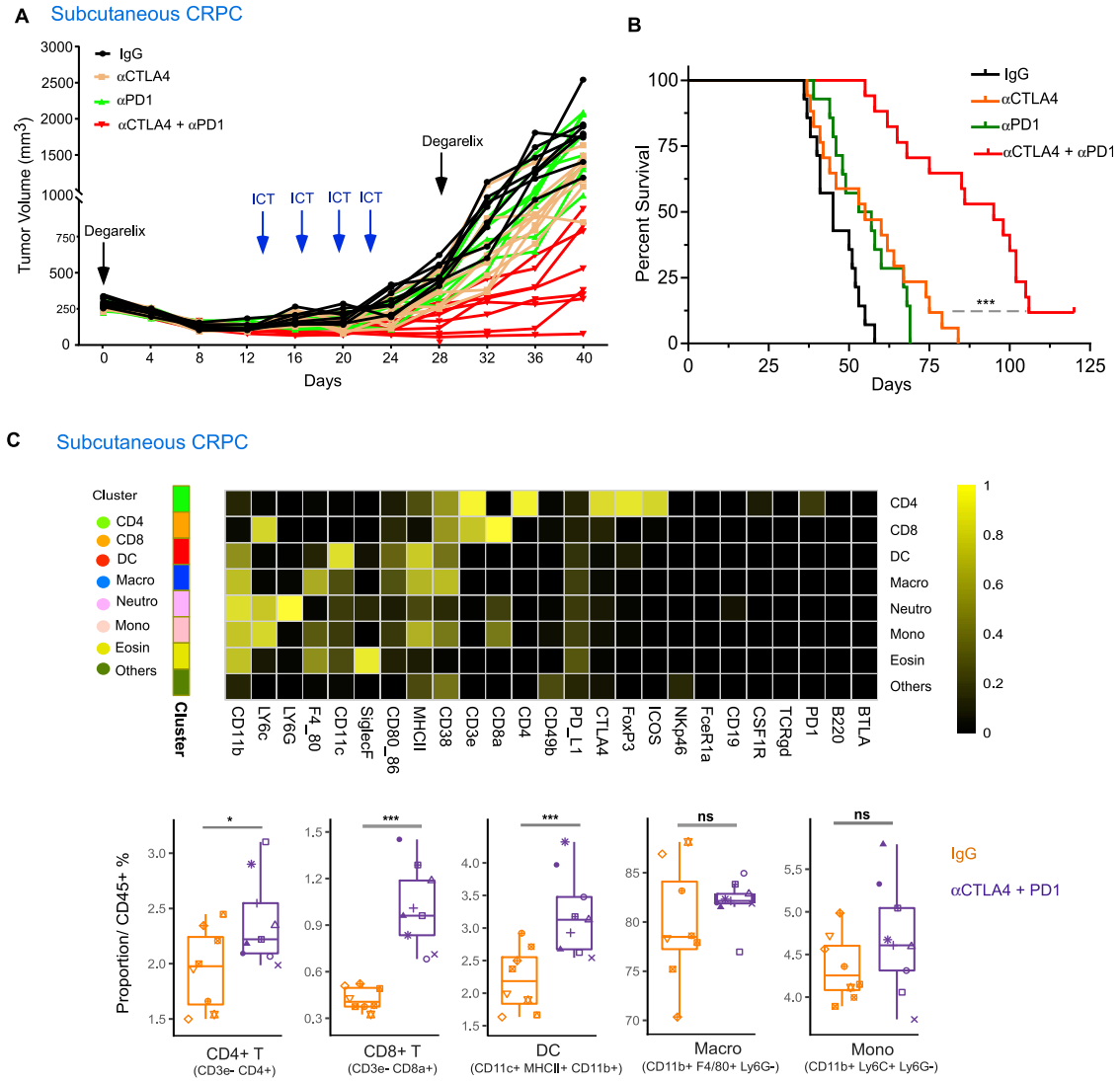

Figure S3. ICT Inhibits Subcutaneous CRPC and Improves the Overall Survival, Related to Figure 2

Shown in (A) is a therapy schedule and subcutaneous CRPC tumor growth curve and in (B) is the overall survival in response to mono- and combination therapies; at the top of (C) is a heatmap showing immune-phenotype of each annotated cluster of CD45$^+$ tumor-infiltrating immune cells in the subcutaneous tumor. On the bottom of (C) is the proportion of each annotated CD45$^+$ subset in subcutaneous CRPC of individual IgG- and ICT-treated mice. Data are represented as median ± interquartile range. *$p < 0.05$, **$p < 0.01$, ***$p < 0.001$; ns, not significant.

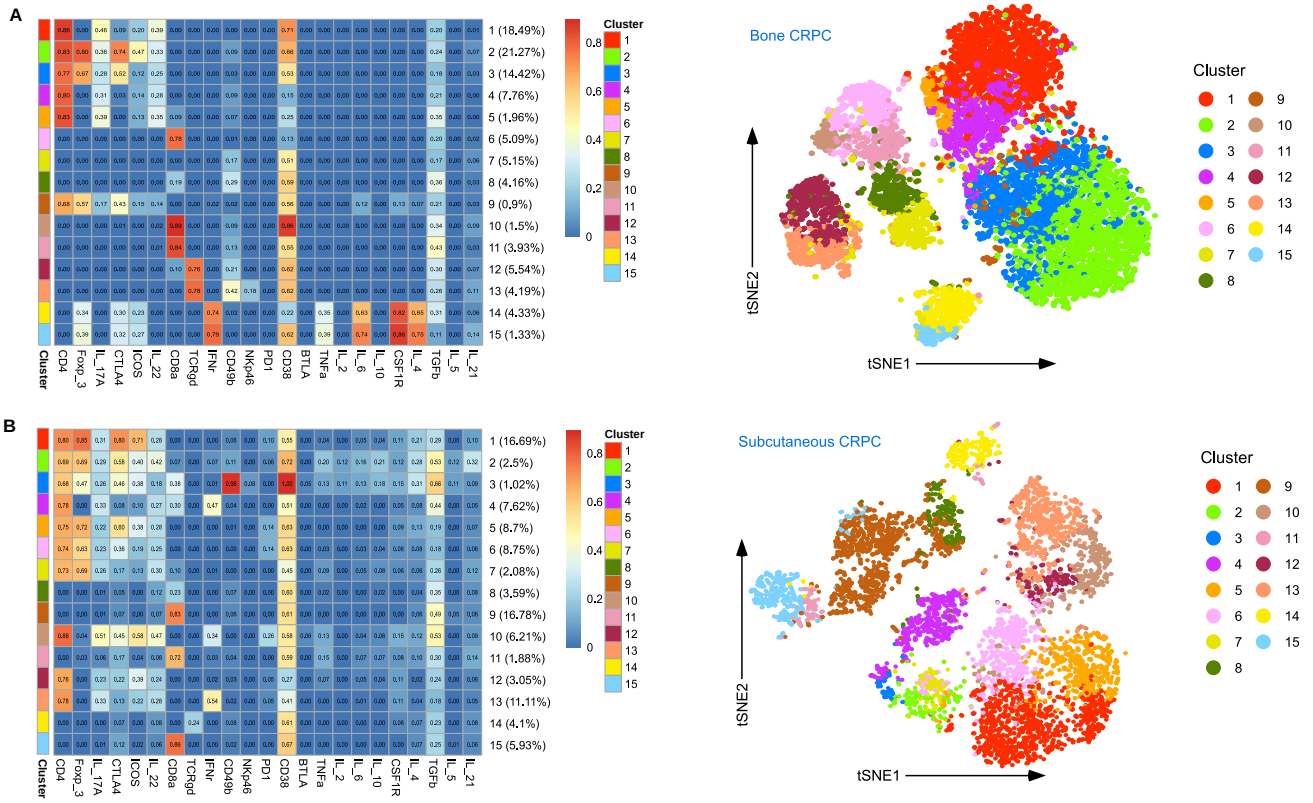

Figure S4. Lack of T_h1 Lineage in Bone CRPC Tumors.

(A and B) CyTOF mapping of tumor-infiltrating CD3ε$^+$CD11b$^-$ T cells in (A) bone and (B) subcutaneous CRPC. Left panel - Heatmap displaying gene expression signature of 15 clusters generated by FlowSOM analysis. Right panel - TSNE visualization of the 15 clusters. The merged and annotated cell subset are shown in Figure 3.

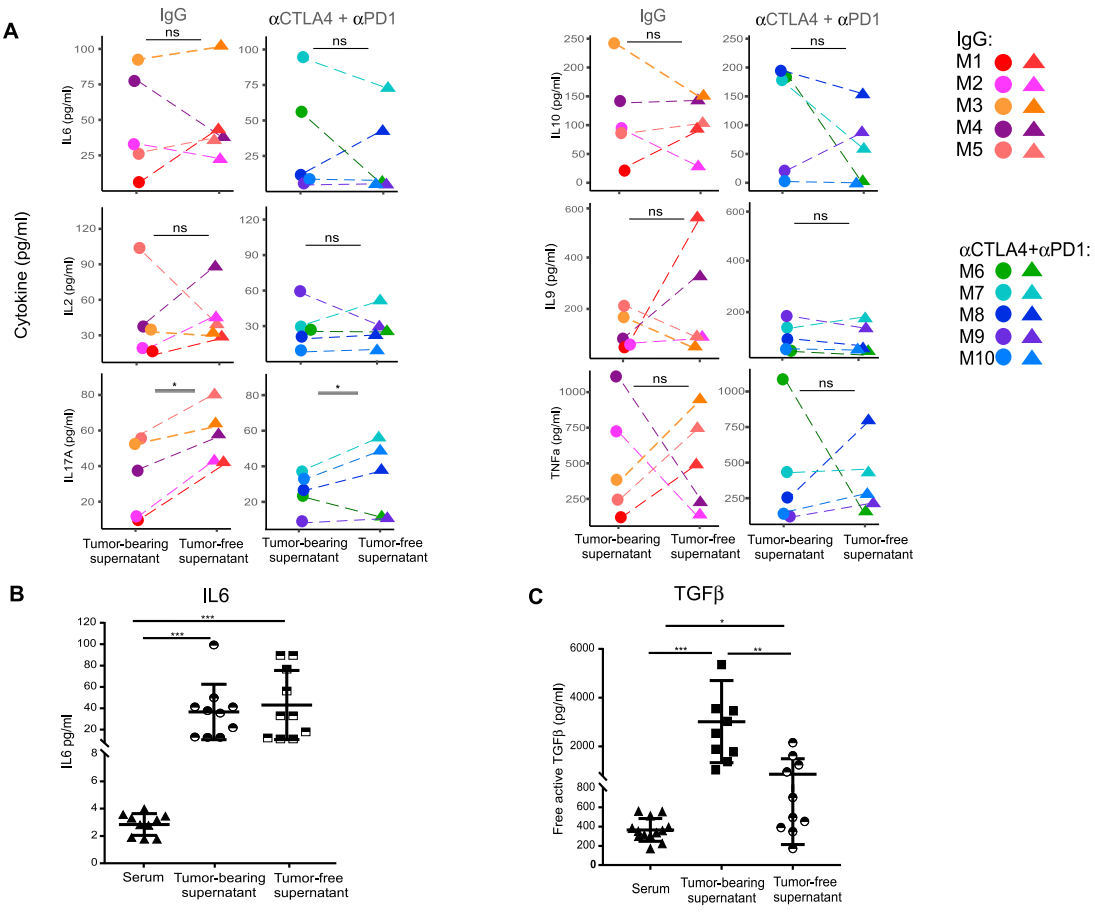

(legend continued on next page)

Figure S5. Cytokine Profiles of the Supernatants of Tumor-Bearing, Contralateral Tumor-Free Bone Marrow, Subcutaneous Tumors and Sera, Related to Figure 4

(A) Levels of the remaining cytokines in the tumor-bearing and contralateral tumor-free supernatants of individual IgG- and ICT-treated mice. The supernatant samples were diluted 1:8 with matrix B provided in the kit. The IL4, IL5, IL12, IL21, IL23 and IFNγ levels were non-detectable or below the detection threshold in most of the samples.

(B and C) The comparative analysis of IL-6 (B) and TGF-β (C) in the sera, and the tumor-bearing and contralateral tumor-free supernatants.

(D) Levels of the remaining cytokines in the serum and the supernatants of bone tumor and subcutaneous tumor from the same mouse (n = 7). Non-osseous: the supernatants of subcutaneous prostate tumors. Osseous: the supernatant of bone tumors. Data are represented as median ± interquartile range. The supernatant samples were diluted 1:4 with matrix B provided in the kit. The IL4, IL5, IL10, IL21 and IFNγ levels were non-detectable or below the detection threshold in most of the samples.

*$p < 0.05$, **$p < 0.01$, ***$p < 0.001$; ns, not significant.

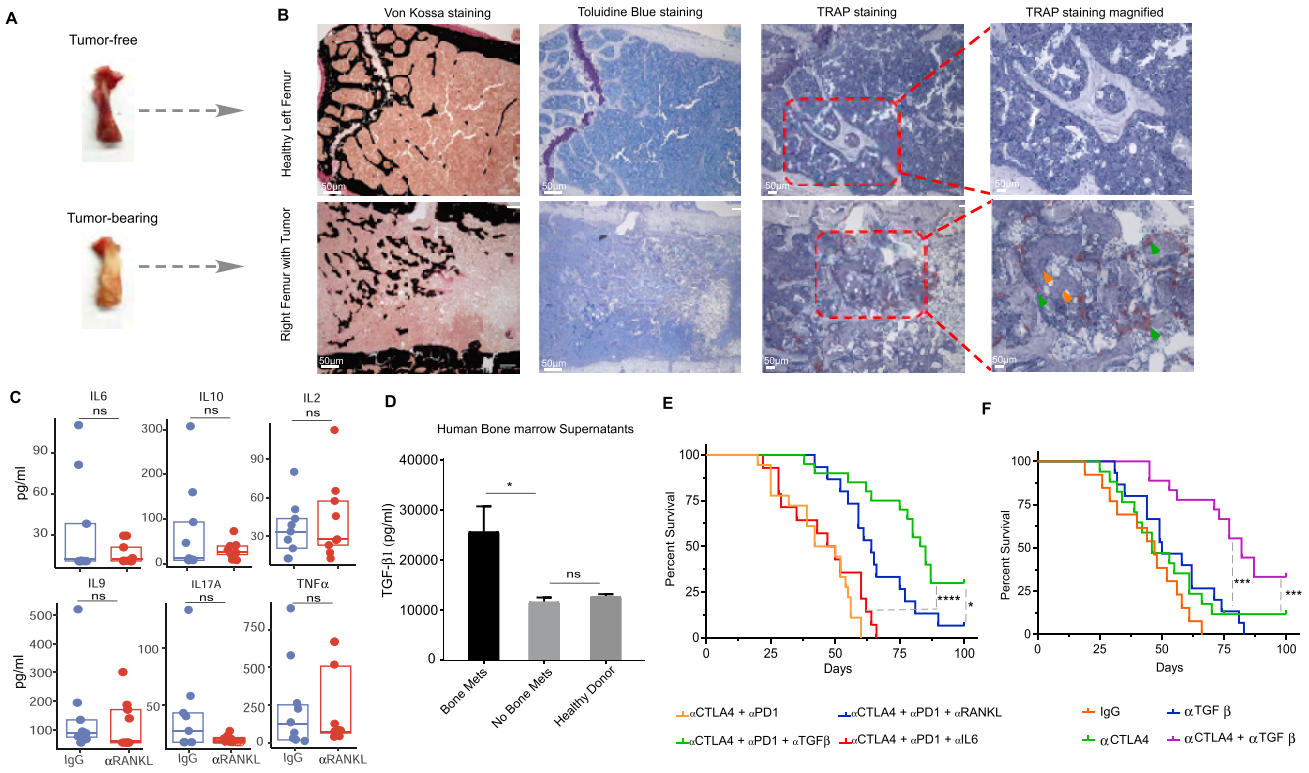

Figure S6. Increased Osteoclastic Activity Elevated TGF-β1 Levels in the Microenvironment of Bone CRPC Lesions, and the Addition of αTGF-β Therapy Improved the Overall Survival of the Mice, Related to Figures 4 and 5

(A) Representative macroscopic images of tumor-free and tumor-bearing femurs from the same mouse.

(B) Representative images of Von Kossa, toluidine blue and TRAP-stained tumor-free and tumor-bearing bone sections. The green and yellow arrows indicate osteoclasts and tumors, respectively. The Oc. S/BS (% bone surface covered with osteoclasts) for tumor-free and tumor-bearing femurs were 2.72% and 6.31%, and the Ob. S/BS (% bone surface covered with osteoblasts) were 1.81% and 14.95%, respectively.

(C) Levels of the remaining cytokines in the tumor-bearing bone marrow supernatants of the IgG- and anti-RANKL-treated mice. The supernatant samples were diluted 1:8 with matrix B provided in the kit. The IL4, IL5, IL12, IL21, IL23 and IFNγ levels were non-detectable or below the detection threshold in most of the samples. Data are represented as median ± interquartile range. *$p < 0.05$, **$p < 0.01$, ***$p < 0.001$; ns, not significant.

(D) Comparative analysis of TGF-β1 levels in the bone marrow supernatants of 4 patients with bone metastases, 4 patients without bone metastases from the clinical trial NCT02703623 and 4 healthy donors. Data are represented as mean ± SEM. *$p < 0.05$, **$p < 0.01$, ***$p < 0.001$; ns, not significant.

(E and F) Survival Analysis of Bone CRPC Mice Subjected to Different Treatments. (E) Overall survival of bone CRPC mice in response to ICT + anti-TGF-β/anti-IL-6/anti-RANKL. (F) Overall survival of bone CRPC mice treated with IgG control, anti-CTLA-4, anti-TGF-β, and their combination.

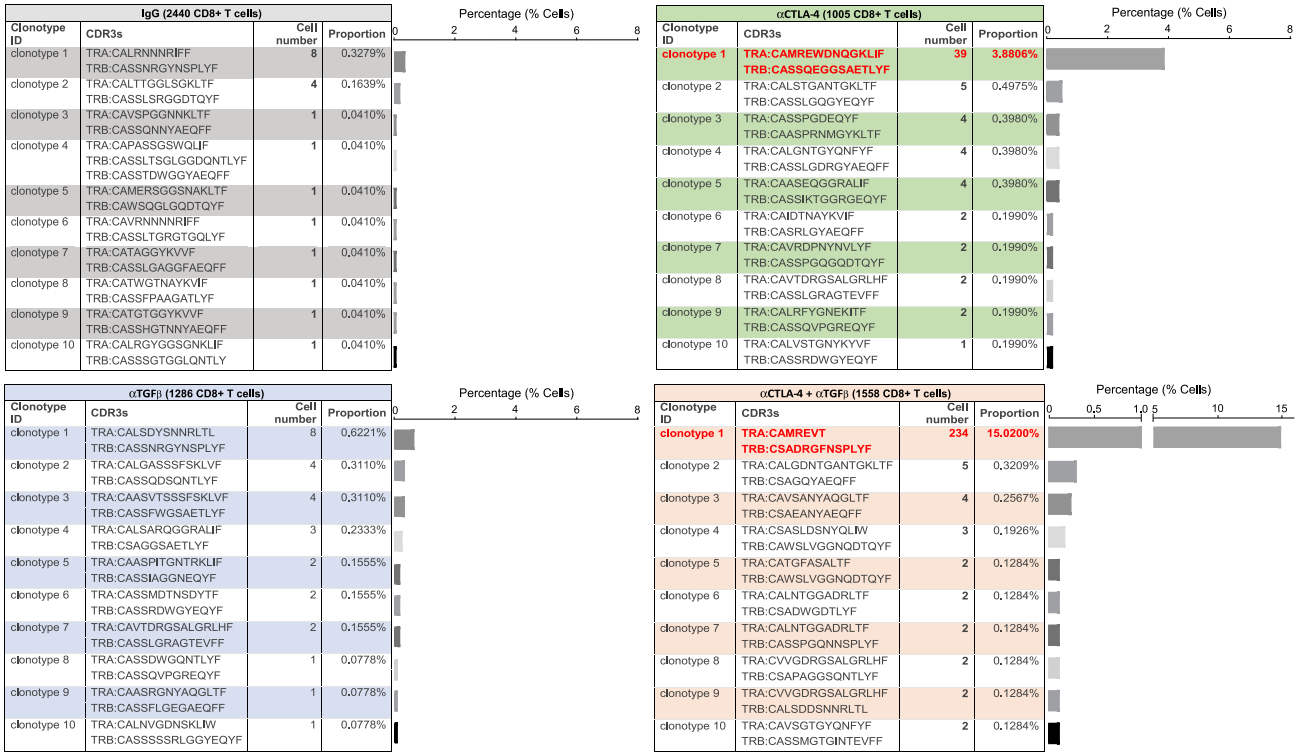

Figure S7. TGF-β Blockade Augments Antigen-Specific Effector / Memory CD8+ T Cell Clonal Expansion in Bone CRPC, Related to Figure 6

Top10 clonotypes of intra-tumoral CD8+ T cells from IgG-treated, anti-CTLA-4, anti-TGF-β, and their combination-treated bone CRPC,